Received: 8 July 2021 | Revised: 18 November 2021 | Accepted: 10 December 2021

DOI: 10.1111/acel.13541

Aging Cell WILEY

ORIGINAL PAPER

Chemically induced senescence in human stem cell-derived neurons promotes phenotypic presentation of neurodegeneration

Ali Fathi[1] | Sakthikumar Mathivanan[1] | Linghai Kong[1] | Andrew J. Petersen[1] | Cole R. K. Harder[1] | Jasper Block[1] | Julia Marie Miller[1] | Anita Bhattacharyya[1,2] | Daifeng Wang[1] | Su-Chun Zhang[1,3,4,5]

[1]Waisman Center, University of Wisconsin-Madison, Madison, Wisconsin, USA

[2]Department of Cell and Regenerative Biology, School of Medicine and Public Health, University of Wisconsin-Madison, Madison, Wisconsin, USA

[3]Department of Neuroscience, School of Medicine and Public Health, University of Wisconsin, Madison, Wisconsin, USA

[4]Department of Neurology, School of Medicine and Public Health, University of Wisconsin, Madison, Wisconsin, USA

[5]Program in Neuroscience and Behavioral Disorders, Duke-NUS Medical School, Singapore, Singapore

Correspondence
Su-Chun Zhang, Waisman Center, School of Medicine and Public Health, University of Wisconsin-Madison, Madison, WI 53705, USA.
Email: suchun.zhang@wisc.edu

Funding information
National Institute of Child Health and Human Development, Grant/Award Number: HD076892 and U54 HD090256; Aligning Science Across Parkinson's, Grant/Award Number: ASAP-000301; National Institute of Mental Health, Grant/Award Number: MH100031; National Institute of Neurological Disorders and Stroke, Grant/Award Number: NS086604 and NS096282; Amyotrophic Lateral Sclerosis Association, Grant/Award Number: 20-IIP-556

Abstract

Modeling age-related neurodegenerative disorders with human stem cells are difficult due to the embryonic nature of stem cell-derived neurons. We developed a chemical cocktail to induce senescence of iPSC-derived neurons to address this challenge. We first screened small molecules that induce embryonic fibroblasts to exhibit features characteristic of aged fibroblasts. We then optimized a cocktail of small molecules that induced senescence in fibroblasts and cortical neurons without causing DNA damage. The utility of the "senescence cocktail" was validated in motor neurons derived from ALS patient iPSCs which exhibited protein aggregation and axonal degeneration substantially earlier than those without cocktail treatment. Our "senescence cocktail" will likely enhance the manifestation of disease-related phenotypes in neurons derived from iPSCs, enabling the generation of reliable drug discovery platforms.

KEYWORDS
cell senescence, disease modeling, neural differentiation, neurodegeneration

Ali Fathi and Sakthikumar Mathivanan are contribute equally.

1 | INTRODUCTION

As global life expectancy increases, neurodegenerative disorders are predicted to cause a staggering burden to society. Substantial efforts have been made to develop effective therapies, but progress is slow and drugs developed based on animal studies have so far mostly failed in clinical trials (Mitsumoto et al., 2014; Paganoni et al., 2014). Poor clinical translatability of animal models necessitates additional models to test therapeutic strategies.

Human pluripotent stem cell (hPSC)-derived neurons model early stages of neurodegeneration and have potential benefits in drug discovery and testing. An advantage of the hPSC model is the ability to capture the human genetic background underlying diseases by establishing patient-specific iPSCs, or by studying specific effects of disease proteins via introducing disease-related mutations into otherwise normal hPSCs (Chen et al., 2014; Sances et al., 2016). However, the iPSC reprogramming process erases many of the aging marks found in somatic donor cells (Lapasset et al., 2011; Menendez et al., 2011; Miller et al., 2013; Rando & Chang, 2012), and hPSC-derived neurons are similar to those in fetal development, based on transcriptional and functional profiling (Nicholas et al., 2013; Patterson et al., 2012; Vera & Studer, 2015). Thus, generating hPSC-derived neurons that resemble those in the adult and aging brain is critical for modeling neurodegenerative diseases using hPSCs.

One approach for modeling cellular senescence (CS) is transdifferentiation of fibroblasts or other aged somatic cells into neurons, avoiding the pluripotent stage and maintaining senescence markers (Mertens et al., 2015; Vierbuchen et al., 2010). Indeed, a recent study showed that transdifferentiated neurons retain age-related transcription profiles and manipulation of RANBP17 was able to reverse some of the age-related transcriptional changes in iPSC-derived neurons (Mertens et al., 2015). However, direct conversion of fibroblasts into neurons is relatively low throughput given the lack of expansion capacity of the resulting neurons.

Modulation of genes linked to premature aging disorders is another strategy to accelerate aging in stem cell models. The ectopic expression of progerin, a mutant form of nuclear lamina protein A (LMNA) that causes accelerated aging in progeria, in an iPSC model of Parkinson's disease (PD) can trigger age-related and degenerative phenotypes, including neuromelanin accumulation, dendrite degeneration, loss of tyrosine hydroxylase, and accumulation of pathological aggregates (Miller et al., 2013). It remains to be determined how closely these approaches model physiological aging in normal neurons or pathological aging seen in late-onset diseases. Overexpression of premature aging genes introduces the challenge of distinguishing phenotypes related to the disease from those induced by foreign gene overexpression.

In the present study, we screened for chemicals/pathways that selectively trigger senescence phenotypes in primary neonatal fibroblasts and iPSC-derived cortical neurons. To identify pathways important in neuronal senescence, we first used transdifferentiated neurons from aged and young fibroblasts and identified molecular markers for neuronal aging, including decreased expression of H3K9Me3, chromatin-associated protein HP1γ, and lamina-associated polypeptide Lap2β. We then used these readouts for screening small molecules and developed a combination of molecules that induce senescence and protein aggregation in cortical neurons differentiated from hPSCs. We evaluated this chemical-induced senescence (CIS) approach in motor neurons (MNs) derived from ALS (TARDBP mutant) patient iPSCs and confirmed that CIS promoted earlier and consistent manifestation of disease-related phenotypes. Furthermore, using autophagy activator molecules, we were able to mitigate CS phenotypes in the MNs. Thus, this CIS strategy enables more effective iPSC modeling of phenotypes in ALS.

2 | RESULTS

2.1 | Identification of small molecules that induce senescence in neonatal fibroblasts

Primary human fibroblasts retain age-related markers depending on the age of the individual from which the cells are isolated (Childs et al., 2015). These cells are thus appropriate reference for studying CS. We compared neonatal fibroblasts with those from a 72-year-old male and 62-year-old female donors by examining the expression of age-related markers H3K9Me3, Lap2β, and HP1γ. We found that neonatal fibroblasts expressed a higher level of H3K9Me3, Lap2β, and HP1γ than old fibroblasts (72 years) in our high-content imaging platform. In addition, the old fibroblasts expressed the senescence-associated β-Gal (Figures 1a,b and S1A-C). These findings are consistent with a previous observation (Miller et al., 2013), indicating that these markers are reliable readouts for assessing CS.

We then looked for molecules that may induce senescence phenotypes in the neonatal fibroblasts, focusing on the known senescence associated pathways. We selected 25 small molecules known to affect pathways involved in CS (Petrova et al., 2016), including autophagy-related molecules, Akt signaling, and inhibitors of mTOR, HDAC, ZMPSTE24, and Sirtuin signaling (Table S1). We examined the toxicity of these molecules in their minimum effective

FIGURE 1 Identifying small molecules for inducing CS in human neonatal fibroblasts. (a) Immunostaining for H3k9Me3, Lap2β, and HP1γ proteins in both neonatal and aged fibroblasts. Scale bar = 100 μm. (b) Frequency distribution for different bins of signal intensity in high-content imaging for H3k9Me3, Lap2β, and HP1γ proteins in male neonatal and aged (72 years old) fibroblasts. (c) Frequency distribution for H3k9Me3, Lap2β, and HP1γ protein expression in male neonatal fibroblasts treated with different small molecules; dashed red line is control, and top seven molecules for each protein are shown in the graph. (d) Mean difference in signal intensity for all 25 small molecules depicted as mean ± 95% confidence intervals compared to the DMSO control group. The zero line means no difference compared to control and if the difference does not touch the reference line then the changes in expression are significant ($n = 4$, t test compared to the control DMSO)

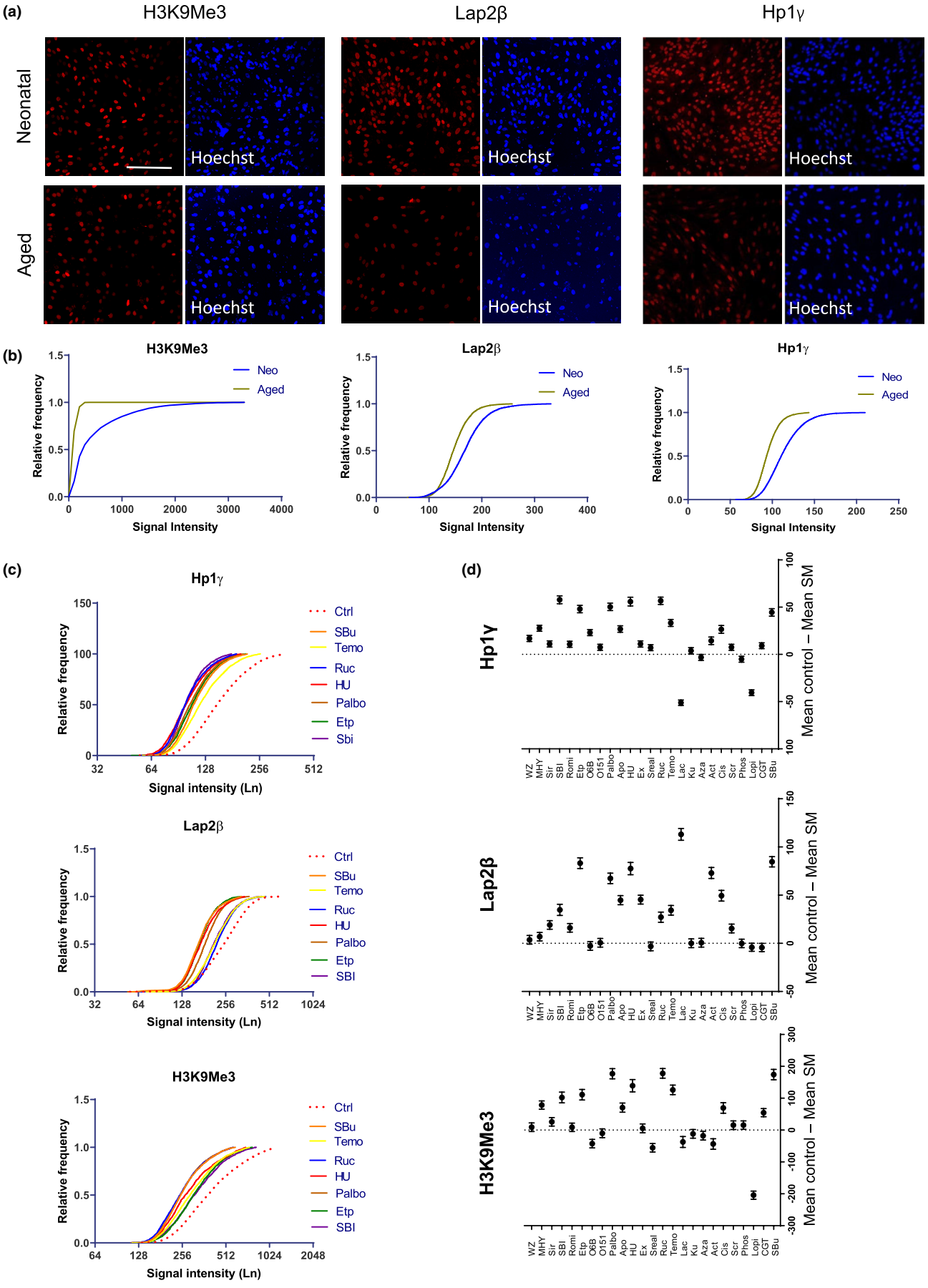
(a)
H3K9Me3
Lap2β
Hp1γ
Neonatal
Aged
Hoechst
(b)
H3K9Me3
Lap2β
Hp1γ
Neo
Aged
Relative frequency
Signal Intensity
(c)
Hp1γ
Lap2β
H3K9Me3
Ctrl
SBu
Temo
Ruc
HU
Palbo
Etp
Sbi
SBI
Signal intensity (Ln)
(d)
Hp1γ
Lap2β
H3K9Me3
Mean control – Mean SM
WZ
MHY
Sir
SBI
Romi
Etp
O6B
O151
Palbo
Apo
HU
Ex
Sreal
Ruc
Temo
Lac
Ku
Aza
Act
Cis
Scr
Phos
Lopi
CGT
SBu

concentrations based on previous studies using calcein AM and ethidium homodimer (EthD-1) fluorescent dyes to distinguish live versus dead cells. None of the small molecules induced cell death beyond the DMSO control (5%–10% cell death) at the final selected concentration (Figure S1D). By culturing the neonatal fibroblasts in the presence of the small molecules at an effective dose for five consecutive days and examining the expression of the above CS markers, we found that more than half of the molecules (13 molecules, $p \leq 0.001$, Table S2) significantly decreased the expression of all three readouts (Figure 1c,d). Among the 13 molecules, seven also induced expression of β-Gal, another consensus marker for CS (Figure S1E,F). Thus, we identified a set of small molecules that induce senescence phenotypes in neonatal fibroblasts.

2.2 | Identifying small molecule cocktails that enhance neuronal senescence

Epigenetic marks, including those associated with aging, are largely erased during reprogramming to iPSCs (Lo Sardo et al., 2017; Rando & Chang, 2012). Consequently, cells differentiated from iPSCs, including neurons, behave like those in embryonic development. In contrast, neurons directly converted from fibroblasts by forced expression of transcription factors retain much of the age-related signatures in their parental somatic cells (Mertens et al., 2015). To validate this phenomenon and to establish CS readouts in neurons, we reprogrammed both young and old human fibroblasts to neurons using a combination of gene overexpression and small molecules (Mertens et al., 2015). Both neonatal and aged fibroblasts were transduced with lentiviral particles for Eto and XTP-Ngn2:2A:Ascl1 (N2A) and cultured in the presence of G418 and puromycin for at least three passages. Induced neurons (iNs), exhibiting polarized morphology and expressing neuronal proteins like β-III tubulin (Figure 2a), appeared at the 2nd week in the neonatal fibroblast group and mostly at the 3rd week for the old fibroblast group. At the end of 3 weeks of DOX treatment, the mean conversion rate for neonatal iNs was 18.1% ± 3.5, whereas for aged iNs was 39% ± 4.4, which were used for further experiments without any purification (Figure 2b). Importantly, the iNs from old fibroblasts showed a lower intensity in the epigenetic mark H3K9Me3, Lamin B2, and Lap2β as well as the heterochromatin protein HP1γ (Figure 2c). Besides the above markers, the morphology and size of a cell and nucleus may serve as a sign of CS (Zhao & Darzynkiewicz, 2013). We also noticed that neonatal iNs had a lower Hoechst (nuclear) intensity (Figure 2d) and a smaller nucleus area compared to their aged counterparts (Figure 2e), while there were no differences in the nuclear roundness and ratio between young iNs and aged iNs (Figure 2f,g). Our results confirmed that the iNs from aged fibroblasts retain the age-related signatures of their parental cells, setting a reference for us to examine the effects of small molecules on CS in embryonic neurons.

Neurons differentiated from ESCs and iPSCs resemble those during embryonic development. To identify small molecules that induce CS in the embryonic neurons, we generated cerebral cortical neurons from GFP-expressing hESCs (H9, WA09) according to an established protocol (Qi et al., 2017; Figure S2). The ESC-derived cortical progenitors at Day 14 expressed SOX1 (86.7%) and OTX2 (87%), markers of cortical progenitors (Figure S2B). When differentiated to mature neurons in the presence of compound E that inhibits notch signaling and MEK inhibitor PD0325901 at Day 21, the majority of the cells expressed neuronal markers (MAP-2b 95%, TUBB3 95%; Figure S2C). Following treatment of the neuronal cultures with small molecules for 4 consecutive days, we assayed for CS hallmarks (Figure S2D). The criteria for positive molecules were defined by expression of CS markers without inducing obvious DNA damage and cell death. By using three different concentrations based on the half maximal inhibitory concentrations (IC50s) for each small molecule, we identified a concentration that did not cause cell death (Figure S2E). Romidepsin, O151, SBI-0206965, Lopinavir, Sodium Butyrate, SCR-7, and Phosphoramidon had a significant impact on the expression of all three readouts H3K9Me3 (mean ± SEM 1980 ± 22, 1957 ± 19, 1632 ± 15, 1806 ± 27, 1990 ± 18, 1908 ± 23, 2037 ± 24, respectively, compared to 2183 ± 14 in control), Lap2β (742 ± 6.4, 688 ± 6, 726 ± 5, 709 ± 8, 734 ± 5, 693 ± 7.7, 855 ± 7.5, respectively, compared to 789 ± 4 in control), and HP1γ (122 ± 3.6, 98 ± 0.5, 92 ± 0.3, 96 ± 0.64, 98 ± 0.5, 99 ± 0.5, 95 ± 0.5, respectively, compared to 108 ± 0.5 in control; Figure 3a,b; Table S2). Romidepsin induced a greater expression of HP1γ and Phosphoramidon induced greater Lap2β expression compared to the mean expression in the control group and were excluded from further experiments (Table S2). Among the remaining molecules, we found that neurons treated with actinomycin D, etoposide, temozolomide, and hydroxy-urea showed higher H2A.x expression compared to the control group (Figure 3c,d), suggesting that these molecules caused significant DNA damage, promoting us to exclude these molecules from further screenings. Five molecules (O151, SBI-0206965, Lopinavir, Sodium Butyrate, and SCR-7) were selected for further analysis.

Our next step was to identify whether any combination of these five small molecules induces CS in neurons. We used the single molecule treatment with SBI-0206965 (autophagy inhibitor) as a reference since it had greater performance in modulating all three readouts during the initial screening. In this set of experiments, we used 50% of the concentration that we used for the first set of experiments for molecules used in pairs and 70% reduction in triple combination to minimize cell toxicity. Results showed that most of the combinations had greater or similar effect to SBI (Figure 4a). Two of the combinations, SLO (SBI-0206965, Lopinavir, O151) and SSO (SBI0206965, Sodium Butyrate, O151), had a greater mean difference in H3K9Me3 and Lap2β expression compared with both DMSO (Control) and SBI-0206965 treated cells ($p < 0.01$).

To determine the minimum period of treatment needed to induce stable CS, differentiated cortical neurons at Day 7 were treated with the SLO small molecules for different periods of time (treated at Day 7, Day 9, Day 10, Day 12, and Day 13) and the cells were analyzed at Day 14. Expression of H3K9Me3, HP1γ, and Lap2β indicated that 2–4 days of continuous treatment with SLO molecules resulted in the maximum effect (Figure 4b–f). This experiment showed that

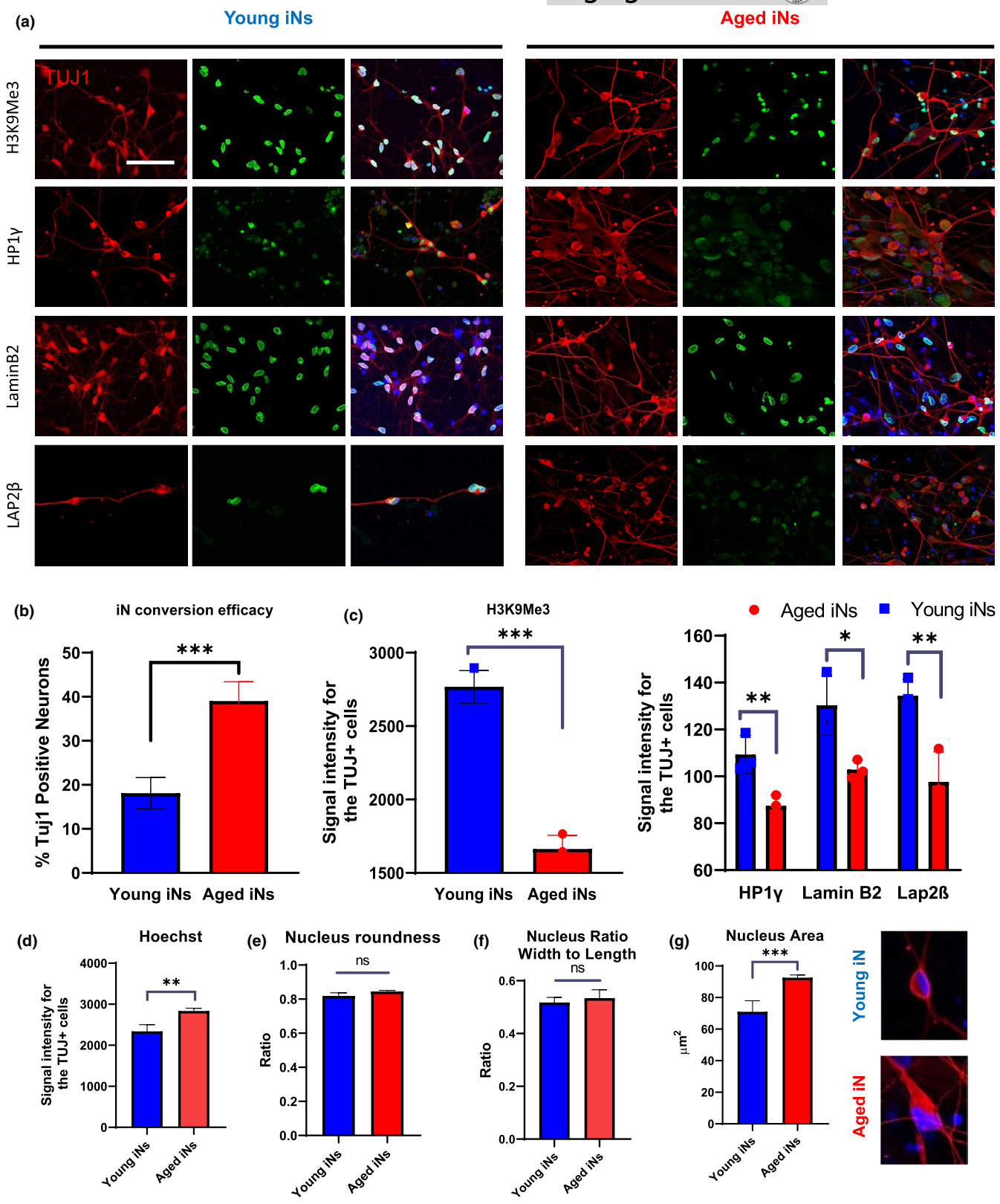

FIGURE 2 Cellular senescence marks are preserved during direct reprograming of fibroblasts to neurons. (a) Immunostaining for H3K9Me3, LaminB2, Lap2β, and HP1γ co-stained with TUJ1 (red) in induced neurons (iNs) derived from fibroblasts of neonatal and a 72-year-old donor. Scale bar = 100 µm. (b) Percentage of TUJ1-positive neurons. (c) Mean signal intensity for H3K9Me3, Lap2β, LaminB2, and HP1γ. (d) Hoechst signal intensity, (e) nucleus roundness, (f) nucleus ratio, and (g) nucleus area for both young and aged iNs (n = 3–10, ns: not significant, *$p < 0.05$, **$p < 0.01$, ***$p < 0.001$ unpaired t test). Note that the representative images of Hoechst and Tuj1 staining for young and aged iNs are placed after D-G

expression of H3K9Me3 and Lap2β at 5- and 7-day post-treatment recovered slightly but not to the level of the DMSO condition. Reduction in HP1γ level was more persistent following SLO treatment and stayed at a lower level compared to the control cells even at 5- and 7-day post-treatment (Figure 4b–f). Downregulation of all three senescence-related proteins, H3K9Me3, HP1γ, and Lap2β, was confirmed by Western blot in the differentiated cortical neurons treated with SLO at Day 7 (Figures 4g,h and S7A-D).

In addition to the CS phenotypes analyzed above, neuronal senescence is often accompanied by intracellular protein aggregation. We hence examined the effect of the top two small molecule combinations on protein aggregation with MG-132-treated cells (a proteasome inhibitor) as a positive control. Proteostat™ staining revealed protein aggregates in cells treated with SSO or SLO comparable to MG-132 condition which was colocalized by Lamp2-positive autophagosomes (Tukey's multiple comparison MG-132 $p < 0.0001$, SLO $p < 0.004$, SSO $p < 0.035$; Figure 4i,j). As additional controls, Proteostat™ and Lamp2 staining revealed more prominent protein aggregation in aged iNs than in the young iNs ($p < 0.003$). Our results show that the CS phenotype in neurons induced by small molecules is associated with intracellular protein aggregation, similar to the phenomena preserved in aged iNs.

Mitochondrial defects are associated with senescence in the directly reprogrammed neurons (Kim et al., 2018). We found that SLO-treated neurons showed a higher ROS level than the control cells, revealed by MitoSoX staining (Figure S3A,C). It is, however, much lower than that in cells treated with FCCP, a potent uncoupler of mitochondrial oxidative phosphorylation and inducer of cell apoptosis. In parallel, JC-10 assay showed that the SLO-treated cortical neurons had a lower mitochondrial membrane potential than untreated controls, but again not as low as that in the FCCP treated cells (Figure S3B,D). Accompanying with the functional changes was morphological alterations in the mitochondria when neurons were treated with SLO, including fewer branches and smaller area for SLO-treated cells, though statistically insignificant (Figure S3E–G). Thus, SLO-induced CS is accompanied by functional alterations in mitochondria, including depolarization and over production of ROS.

2.3 | SLO-treated neurons express CS-related transcripts and pathways

To define CS-related changes in SLO-treated neurons, we performed RNA-seq analysis on cortical neurons treated with or without SLO. Principal component analysis (PCA) based on overall gene expression showed high similarity (clustering) among independently cultured neurons treated with SLO or among those without SLO treatment (controls), but a high degree of separation between the SLO-treated and the control groups (Figure 5a). When comparing our RNAseq data with iNs from both young (<30 years, eight samples) and aged (>60 years, nine samples; Mertens et al., 2015), we found that our cortical neurons are similar to young iNs, whereas the SLO-treated neurons clustered with aged iNs (Figure 5a). We further compared our SLO-treated cells to the aged (>60 year, $N = 205$) and young (<30 year, $N = 128$) brain samples available in PsychENCODE (Wang et al., 2018). The SLO-treated samples (orange dots) are clustered with the PsychENCODE aged group (red dots), whereas the CTRL samples (blue dots) are clustered with the PsychENCODE young group (green dots). Note that we used PC2 and PC3 for showing clustering since the first PC (PC1) likely captures potential major confounding factors between our study and PsychENCODE (Figure 5b). Together, our results indicate that the SLO-treated neurons resemble those in the aged human brain and those directly converted from aged fibroblasts.

We then looked at the human aging scores (−log10(*p*-value) for the genes that are associated with aging, see RNAseq in methods) of cortical neurons treated with SLO. We found that the upregulated genes in SLO-treated cells have higher human aging scores in the PsychENCODE aged group than the downregulated genes (Figure 5c, *t* test $p < 2.2e{-}16$). Similarly, the downregulated genes have significantly higher human aging scores in the PsychENCODE young group than the aged genes (Figure 5d, *t* test $p < 2.2e{-}16$). These results suggest that our SLO-treated neurons have a similar gene expression dynamic to that in the aged human brain in PsychENCODE.

Comparison between SLO-treated neurons and DMSO control neurons resulted in **271** differentially expressed genes (DEGs; FDR < 0.05, 0.6 ≤ logFC ≤ −0.6) with **190** genes downregulated and **81** genes upregulated upon SLO treatment (Figure 5e; Table S3). These DEGs are also present in the gene list that are significantly modulated by age in PsychENCODE (Table S4). In our SLO DEG list, GABA receptors are among the most downregulated genes whereas histone variants are upregulated (Figure 5f). Pathway analysis for DEGs in the SLO-treated neurons revealed that neurotransmitter receptor signaling and GPCR signaling are downregulated whereas pathways in the histone modification (especially histone variants) are upregulated (Figure 5g).

Premature aging syndromes that are associated with mutations in LMNA or WRN genes resemble normal aging in terms of

FIGURE 3 Chemical induction of CS in hESC-derived cortical neurons. (a) Frequency distribution of high-content imaging data for H3K9Me3, Lap2β, and HP1γ proteins in cortical neurons. The dashed red line is control, and top seven molecules for each protein marker are shown in the graph. (b) Mean difference for signal intensity of all 25 small molecules depicted as mean ± 95% confidence intervals compared to the DMSO control. The zero line means no difference compared to the control and if the difference does not touch the reference line then changes in expression are significant. (c) Confocal images of phospho-Histone H2A.X (Serine 139) in the H9-GFP cortical neurons treated with Etoposide, Actinomycin D, and DMSO as control (Scale bar = 50 μm). (d) Quantification results for the number of positive foci for phospho-Histone H2A.X (Serine 139) per nucleus in cortical neurons treated with different small molecules. ($n = 3$, ns: not significant, $^{*}p < 0.05$, $^{**}p < 0.01$, $^{***}p < 0.001$ one-way ANOVA with Dunnett's multiple comparison test)

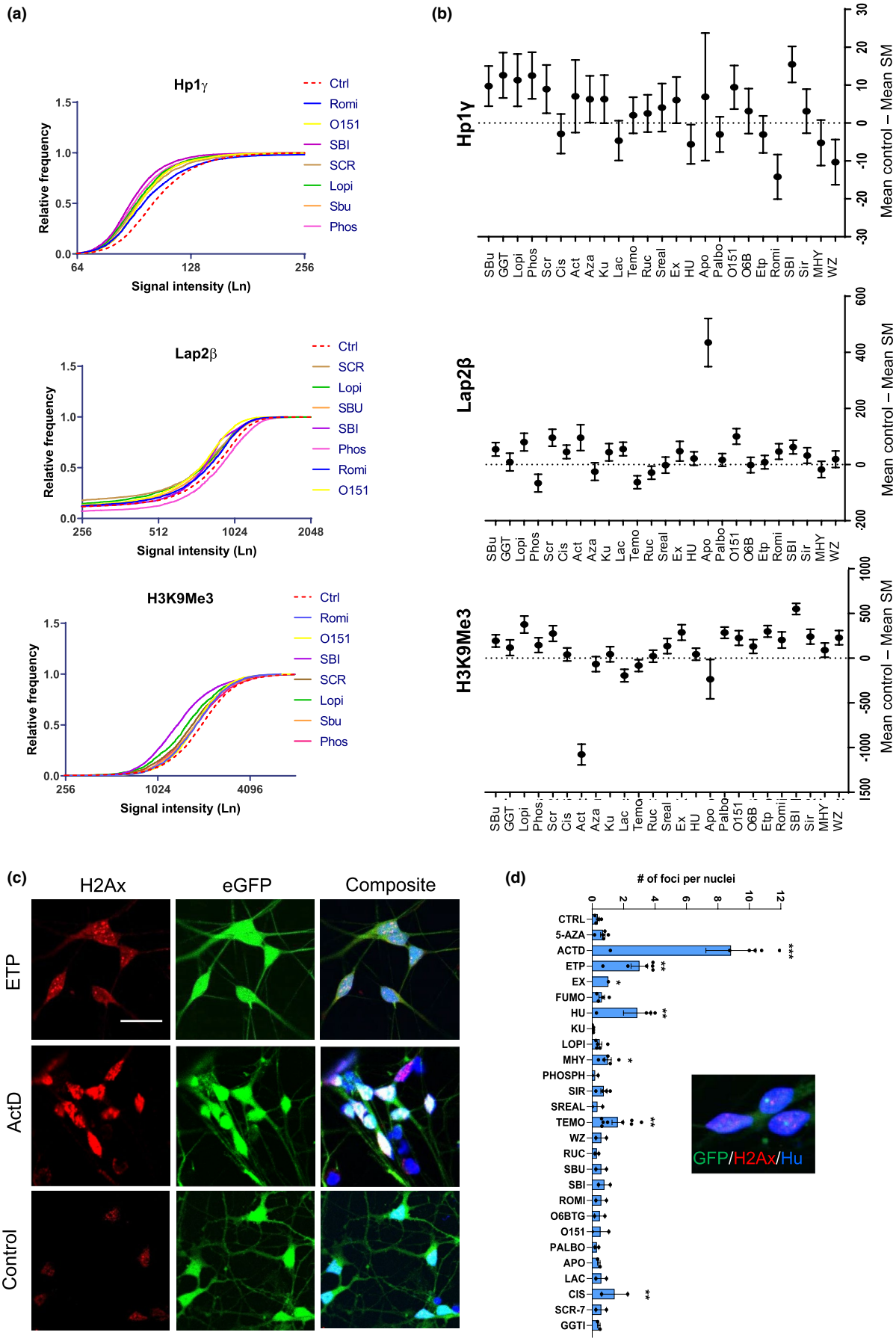
(a)
Hp1γ
Relative frequency
Signal intensity (Ln)
Ctrl
Romi
O151
SBI
SCR
Lopi
Sbu
Phos
Lap2β
Relative frequency
Signal intensity (Ln)
Ctrl
SCR
Lopi
SBU
SBI
Phos
Romi
O151
H3K9Me3
Relative frequency
Signal intensity (Ln)
Ctrl
Romi
O151
SBI
SCR
Lopi
Sbu
Phos
(b)
Hp1γ
Lap2β
H3K9Me3
Mean control – Mean SM
SBu GGT Lopi Phos Scr Cis Act Aza Ku Lac Temo Ruc Sreal Ex HU Apo Palbo O151 O6B Etp Romi SBI Sir MHY WZ
(c)
H2Ax
eGFP
Composite
ETP
ActD
Control
(d)
# of foci per nuclei
CTRL
5-AZA
ACTD
ETP
EX
FUMO
HU
KU
LOPI
MHY
PHOSPH
SIR
SREAL
TEMO
WZ
RUC
SBU
SBI
ROMI
O6BTG
O151
PALBO
APO
LAC
CIS
SCR-7
GGTI
GFP/H2Ax/Hu

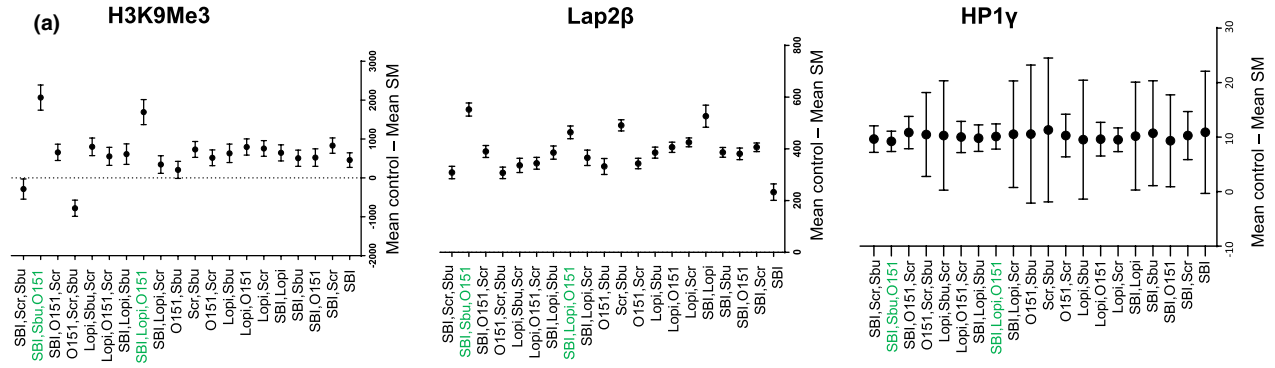
(a)
H3K9Me3
Lap2β
HP1γ
Mean control – Mean SM
SBI,Scr,Sbu
SBI,Sbu,O151
SBI,O151,Scr
O151,Scr,Sbu
Lopi,Sbu,Scr
Lopi,O151,Scr
SBI,Lopi,Sbu
SBI,Lopi,O151
SBI,Lopi,Scr
O151,Sbu
Scr,Sbu
O151,Scr
Lopi,Sbu
Lopi,O151
Lopi,Scr
SBI,Lopi
SBI,Sbu
SBI,O151
SBI,Scr
SBI


(b)
+SLO
Assay at Day14
Day7
Day9
Day11
Day12
Day13
7
5
3
2
1

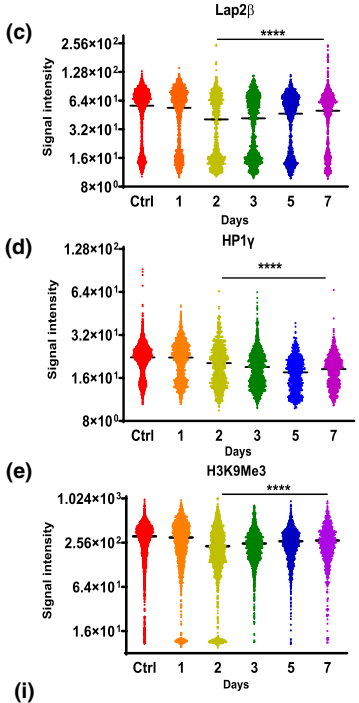
(c)
Lap2β
(d)
HP1γ
(e)
H3K9Me3
Signal intensity
Ctrl
1
2
3
5
7
Days
****

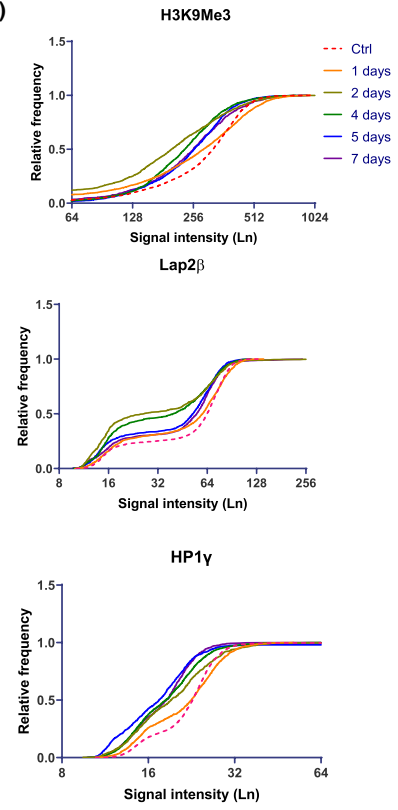
(f)
H3K9Me3
Lap2β
HP1γ
Relative frequency
Signal intensity (Ln)
Ctrl
1 days
2 days
4 days
5 days
7 days

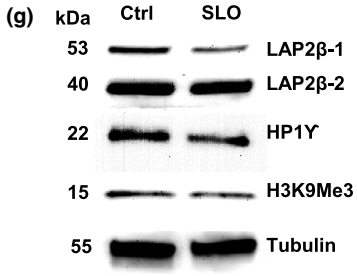
(g)
kDa
Ctrl
SLO
53
LAP2β-1
40
LAP2β-2
22
HP1Y
15
H3K9Me3
55
Tubulin

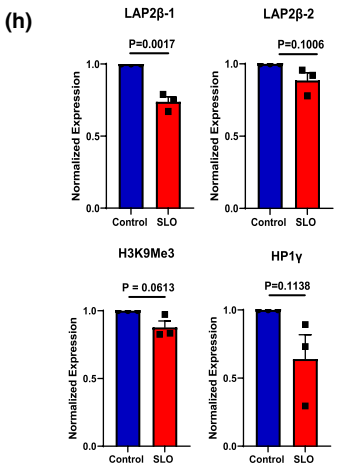
(h)
LAP2β-1
LAP2β-2
P=0.0017
P=0.1006
H3K9Me3
HP1γ
P = 0.0613
P=0.1138
Normalized Expression
Control
SLO

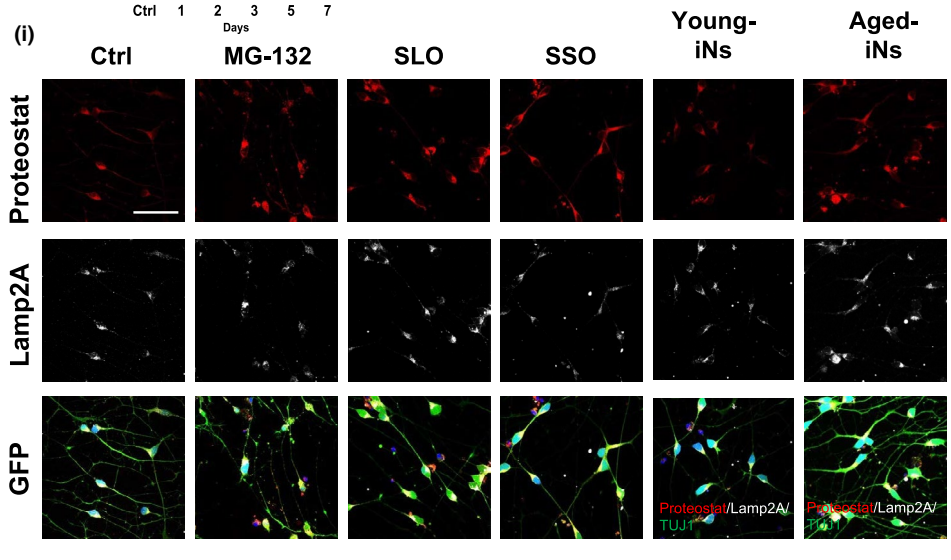
(i)
Ctrl
MG-132
SLO
SSO
Young-iNs
Aged-iNs
Proteostat
Lamp2A
GFP
Proteostat/Lamp2A/TUJ1
Proteostat/Lamp2A/TUJ1

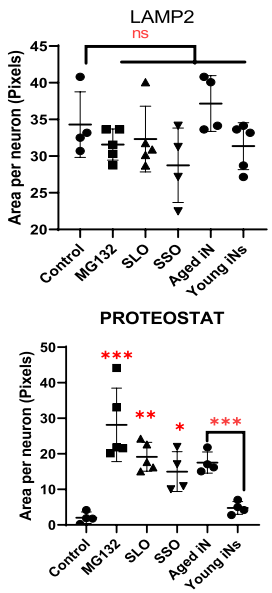
(j)
LAMP2
ns
Area per neuron (Pixels)
Control
MG132
SLO
SSO
Aged IN
Young iNs
PROTEOSTAT
***
**
*
***

FIGURE 4 Combinatorial effect of small molecules on CS in cortical neurons. (a) Different combination of five most effective molecules (O151, SBI-0206965, Lopinavir, Sodium Butyrate, SCR-7) tested on cortical neurons and mean expression of H3K9Me3, Lap2β, and HP1γ in treatment groups compared to the DMSO control. (b) A graph showing the period of SLO treatment on the expression of Lap2β, HP1γ, and H3K9Me3 at Day 14 after maturation and (c–e) high-content imaging quantification of signal intensity for each marker after SLO treatment. (f) Relative frequency distribution of different bins of signal intensity for Lap2β, HP1γ, and H3K9Me3 in cortical neurons treated with different small molecules. (g) Representative images of Western blot for all three markers in cortical neurons treated at Day 21 of differentiation and (h) their normalized protein expression to tubulin expression. (i) Immunostaining images of H9-GFP cortical neurons treated with MG-132 (proteasome inhibitor), SLO (SBI-0206965, Lopinavir and O151), and SSO (SBI-0206965, Sodium Butyrate and O151) and stained for Lamp2A (Lysosome membrane associated protein) and Proteostat dye for detection of protein aggregation (Scale bar = 100 μm), and (j) quantification of positive area in neurons for Lamp2A and Proteostat. (i, j) Young and aged iNs added for comparison with ESC-derived cortical neurons. ($n = 3$, ns: not significant, $^{*}p < 0.05$, $^{**}p < 0.01$, $^{***}p < 0.001$ one-way ANOVA with Dunnett's multiple comparison test). For Western blot quantification, unpaired Student's *t* test was performed

gene expression (Dreesen & Stewart, 2011; Kyng et al., 2003). Overexpression of mutant Lamin A/C (Progerin) in normal neurons causes aging phenotypes (Miller et al., 2013). Interestingly, the SLO-treated neurons exhibited an upregulated pathway (WP4320) that shares 11 genes (30% of total genes in the pathway) involved in Hutchinson–Gilford Progeria syndrome (Figure 5g). They included histone variants, several of which are involved in the histone modification pathway (WP2369). Other transcripts that are upregulated in SLO-treated cells included insulin receptor substrate 1 and 2 (IRS1 and IRS2), pro-apoptotic genes (FOXO3, BAD, and BCL2L11), nutrients sensing transcripts (EIF4EBP1, TSC2, and EEF2) and downstream kinase molecules (PIK3R2, ELK1, PTPRF, MAPK7, AKT1, MAP2K2, PLCG1, CRTC1, and JUN), and other transcripts (SHC2, RAB3A, DOCK3, RELA, NCK2, RACK1, SH2B1, LINGO1, STAT5B, EGR1, and SQSTM1). Other downregulated transcripts in SLO-treated cells included AMPA and NMDA receptors (GRIA1, GRIA2, GRIA3, and GRIN2B), both trkB and trkC receptors (NTRK2 and NTRK3) and their downstream calcium signaling molecules (NFATC4, CAMK2A, and CAMK4), MAPK responsive transcripts (MAP2K1, KIDINS220, PRKAA2, and PPP2CA), and other transcripts (GABRB3, MEF2C, SHC3, RASGRF1, PIK3R1, CDC42, CDH2, CNR1, SPP1, EIF4E, NSF, PTPN11, DLG1, and APC). The transcriptome data suggest that the SLO-treated neurons resemble those from aged human cortex and premature aging samples.

2.4 | Induction of CS accelerates disease phenotype manifestation in ALS MNs

Neurodegenerative diseases such as amyotrophic lateral sclerosis (ALS) usually manifest symptoms after the 5th decade of life. We hypothesized that induction of CS in ALS iPSC-derived neurons would accelerate the presentation of disease phenotypes. We used the *TARDBP* mutant (298S) iPSC line generated from an ALS patient and its isogenic cell line (298G) produced by correcting the mutation using CRISPR (Figure S4). Both mutant and corrected iPSCs were differentiated to spinal MNs using our previously published protocol (Chen et al., 2014; Du et al., 2015; Figure 6a), and the MNs were treated with the SLO cocktail for 4 days. As expected, addition of the small molecules at Day 25 and assayed at Day 28 did not significantly alter the percentage of cells expressing cleaved caspase 3 (Figure 6b), indicating no obvious cytotoxicity for SLO and SSO treatments (control = 26.9 ± 1.3, SLO = 25 ± 2.4, SSO = 24.7 ± 4.9) whereas we found significant number of caspase 3 positive cells in MG132 treated neurons (MG132 = 36.92 ± 1.33).

We then examined if the MNs treated with SLO display CS-like phenotypes as we observed in fibroblasts and cortical neurons. Both 298G and 298S MNs showed a reduction in the expression of H3K9Me3 and Lap2β following SLO treatment (Figures 6c and S6A), indicating that SLO treatment induces CS. Both cell lines responded at the same level to the SLO chemicals, and difference in H3K9Me3 and lap2β signal intensity was not significant (Figure 6c). We then asked if induction of CS accelerates neuronal degeneration. By Day 32, the 298S MNs treated with SLO showed axonal swellings, a sign of axonal degeneration whereas 298G MNs showed relatively intact neurites (Figure 6d). Proteostat staining was increased in SLO-treated cells, especially in the 298S MNs. ALS MNs, when treated with SLO, were positive for phosphor-TDP43 and Proteostat (Figures 6e and S5). Immunofluorescence for phosphorylated neurofilament, a marker for axonal degeneration and turnover, was also significantly increased in the SLO-treated 298S than in non-SLO-treated 298S and SLO-treated 298G MNs. Under higher magnification, Proteostat-positive aggregates were observed along the axons and were positive for both α-internexin and phosphorylated neurofilament (Figures 6e and S5). Quantification of the aggregates showed a significant increase in p-NFH aggregates (1.22 ± 0.31 in 298G compare to 4.26 ± 0.92 in 298S) and Proteostat-positive aggregates (4.49 ± 0.38 in G298G compare to 7.86 ± 1.06 in G298S) in 298S ALS mutant MNs than the 298G isogenic control MNs that were treated with SLO (Figure 6f,g). Following SLO treatment, ALS MNs had significantly more p-TDP43 signal compared to the isogenic control and cells that are not treated with SLO (Figures 6h and S5). We also detected TDP43 signal permeation from nucleus to the cytoplasm area in the ALS MNs and neurons treated with the SLO (Figures 6i and S5). Interestingly, neurite swelling contained p-TDP43 proteins that are colabeled with Proteostat and other neurofilaments are more pronounced in the ALS MNs treated with the SLO (Figures 6e and S5).

One of the hallmarks of neurodegeneration is mitochondrial deficit. Assay with JC-10 staining showed that ALS-MNs had a lower

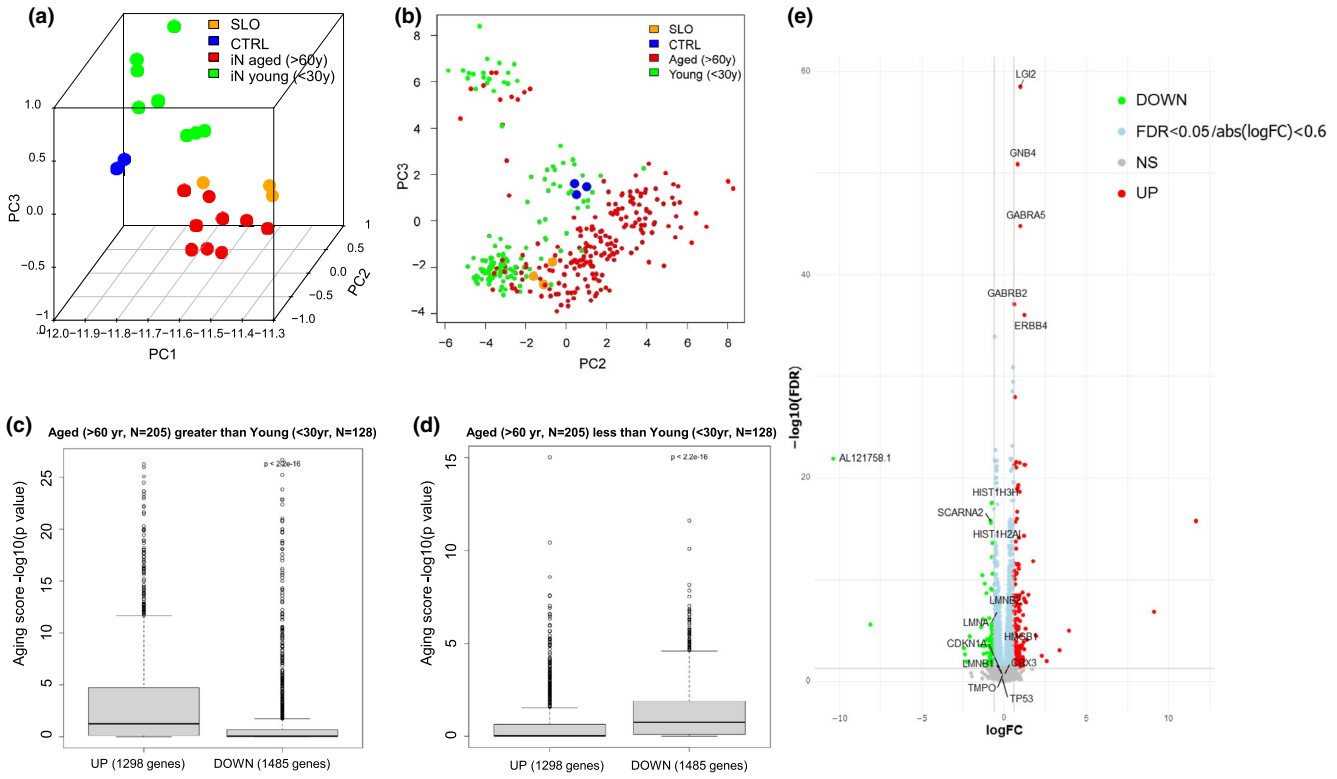

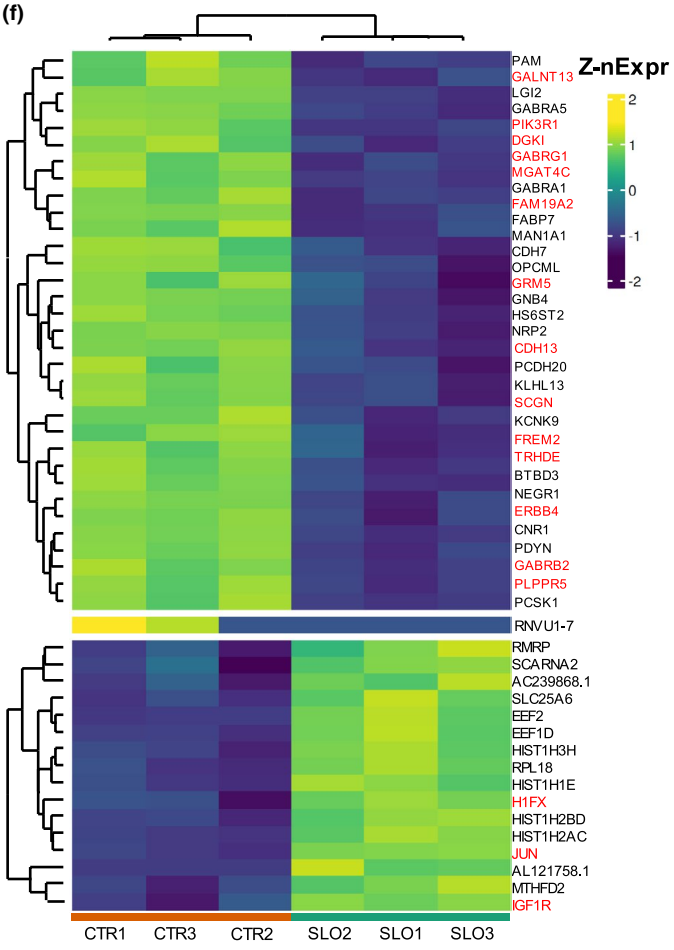

(g)

Overrepresented pathways in SLO

Term	Overlap	P-value	Genes
The effect of progerin on the involved genes in Hutchinson-Gilford Progeria Syndrome WP4320	11/37	1.49E-05	HIST1H2AM;HIST1H2AL;HIST2H2AA4;HIST1H3A;HIST2H4B;HIST1H2AI;HIST1H2AD;HIST1H3H;HIST1H3I;HIST2H3D;HIST1H2AB
Histone Modifications WP2369	11/67	1.58E-04	

Underrepresented pathways in SLO

Term	Overlap	P-value	Genes
GABA receptor Signaling WP4159	6/31	4.10E-07	GABRB2;GABRA1;GABRA5;GABRA4;SLC6A11;GABRG1
Phosphodiesterases in neuronal function WP4222	6/53	1.08E-05	PDE1C;PPP1R1B;PDE3A;ADCY2;CHRFAM7A;PDE7B
Nicotine Activity on Dopaminergic Neurons WP1602	4/21	4.16E-05	KCNK9;CHRNA5;PPP1R1B;ADCY2
Serotonin and anxiety WP3947	3/17	5.20E-04	GABRA1;HTR2C;HTR2A
GPCRs, Class A Rhodopsin-like WP455	8/257	0.003257	MC4R;CHRM5;NPY1R;HTR2C;PRLHR;CXCR4;OPRK1;HTR2A
Monoamine GPCRs WP58	3/33	0.003733	CHRM5;HTR2C;HTR2A
PPAR signaling pathway WP3942	4/67	0.003794	FABP3;CD36;SLC27A2;RXRG
Sudden Infant Death Syndrome (SIDS) Susceptibility Pathways WP706	6/158	0.004051	GABRA1;MAOA;CHRFAM7A;HTR2A;PPARGC1A;PPARGC1B

FIGURE 5 RNAseq analysis on SLO-treated cortical neurons. PCA plot for SLO and CTRL samples as well as induced neurons (iNs) converted from both (a) aged (nine samples) and young (eight samples) fibroblasts and (b) the aged and young PsychENCODE samples (the old group (>60 years, $N = 205$) and the young group (<30 years, $N = 128$)). Boxplots for human aging scores association between SLO neurons and brain samples for (c) upregulated genes and (d) downregulated genes in the aged brains. (e) Smear plot represents each gene with a dot, the gray dots (below cutoff line) are genes with no change relative to the contrast direction, red dots denote upregulated transcripts in the control neurons (with decreased expression in the SLO-treated neurons), and green dots denote downregulated transcripts in the control neurons (upregulated in SLO-treated neurons), respectively, at an adjusted *p*-value (FDR) significance threshold of 0.05. For FDR correction, we used Benjamini–Hochberg method. The light blue dots are transcripts with FDR < 0.05 but have log expression change of less than 0.6. The *x*-axis (log2 fold change) is the effect size, indicating how much expression has changed with SLO treatment. (f) Heatmap clustering for 50 of the most differentially expressed genes with a *p*-value < 0.05 and a log (2) fold-change greater or less than 2. The *Z*-score of a given expression value is the number of standard deviations away from the mean of all the expression values for that gene. (g) All DEGs with a FDR < 0.05 and 0.6 ≤ logFC ≤ −0.6 are selected and tested for over- or under-representation of pathways in the gene list. Any significantly enriched WikiPathway pathways are ordered from most to least significant based on the *p*-value

mitochondrial membrane potential than the isogenic control MNs. Treatment with SLO lowered the membrane potential for control neurons but not further for the ALS-MN (Figure 6j). Morphological analysis with Mitotracker staining showed that isogenic control MNs treated with SLO had shorter and smaller mitochondria than those without SLO treatment, but SLO treatment had no further effect on ALS MNs (Figure S6B-D). Given that mitochondrial DNA is generally not reprogrammed during iPSC generation, these results suggest that the mitochondrial phenotypes are present in ALS-iPSC-derived MNs and that SLO treatment does not appear to exacerbate the mitochondrial phenotypes beyond what are present in ALS-MNs.

2.5 | Autophagy Induction clears up protein aggregation and improves neurite health

The fast and consistent presentation of disease-relevant phenotypes in SLO-induced cultures makes them amenable for testing therapeutic agents. We examined the effects of molecules on protein aggregation and neurite swelling in the SLO-treated ALS MN cultures, including the current ALS medication Edaravone, autophagy activators STF-62247, SMER28, Flubendazole, and the peptide Tat-Beclin, and KU-60019, a molecule identified from our initial cell toxicity screening as neuroprotective. In addition, amiodarone was used as an unrelated hit. MNs from both ALS (298S) and isogenic (298G) iPSCs at Day 28 post-differentiation were treated with SLO and then the compounds were added separately 24 h later, and cells were analyzed at Day 32 (Figure 7a). SMER28 and Tat-Beclin decreased proteostat-positive aggregates in both ALS (37% ± 14 and 62.5% ± 5.5) and isogenic MNs (38% ± 11.7, 66.9% ± 5 for 298G) as compared to SLO-treated control. Edaravone and KU-60019 reduced the level of Proteostat, more so on ALS cells (to 26% ± 6 and 17% ± 0.7) than the isogenic cells (64% ± 10.4, 30% ± 13.6 for 298G). MNs treated with STF-62247 and Flubendazole showed more aggregates in 298G cells compared to the SLO-treated cells (179% ± 29, 143 ± 26.8) and no improvement in 298S cells. Amiodarone did not improve protein aggregation (Figure 7b).

Neurite swelling is one of the obvious morphological changes in ALS MNs following SLO treatment. SMER28 and EDARAVONE significantly reduced the number of swellings to the level of isogenic control cells (Figure 7c). However, KU-60019 treatment did not improve the swelling phenotype to the normal level (Figure 7c) despite significant reduction in protein aggregation (Figure 7b). Other molecules did not show significant improvement in 298S MNs or even induced more swellings in the 298G control cells (Figure 7c). Thus, EDARAVONE and SMER28 can reduce both protein aggregation and neurite swellings in 298S TDP43 mutant cells and were beneficial for MN health in our CS culture system.

3 | DISCUSSION

Most neurodegenerative diseases are concurrent with aging (Baker & Petersen, 2018; Bickford et al., 2017; Duncan, 2011; Sawada et al., 2008). Hence, recapitulating CS in stem cell-derived neurons could expand the capacity of the iPSC model to study disease mechanisms (Mertens et al., 2018; Vernadakis & Fleischer-Lambropoulos, 2000). By using H3K9Me3, HP1γ, and Lap2β as readouts and screening for chemicals/pathways that induce CS in neonatal fibroblasts and iPSC-derived cortical neurons, we developed cocktails of small molecules that induce CS in the cortical neurons. This CIS approach was validated in MNs derived from ALS patient iPSCs. Importantly, CIS enhanced the presentation of disease-related phenotypes. This CIS strategy will likely enable more effective iPSC-based modeling of age-related degenerative diseases and enable better therapeutic target design.

Cellular senescence across different cell types shares features including mitochondrial dysfunction, DNA damage, P16 expression changes, and epigenetic marks for gene silencing (Kim et al., 2018; Madabhushi et al., 2014; Rubinsztein et al., 2011; Satoh et al., 2017). These alterations ultimately result in age-related changes at the cellular level, including changes in cell size, shape and metabolism, proliferation arrest, and telomere erosion (Hernandez-Segura et al., 2018; Lopez-Otin et al., 2013; Petrova et al., 2016). In mitotic cells like fibroblasts, expression of P16 accompanies proliferation arrest and induces senescence (Coppe et al., 2011; Rayess et al., 2012). P16 activation by Palbociclib in our study is one of the most efficient pathways in CS by blocking CDK4/6 and proliferation of fibroblasts, causing senescence. Other pathways in our study with fibroblasts are related to the DNA repair, DNA synthesis, and DNA

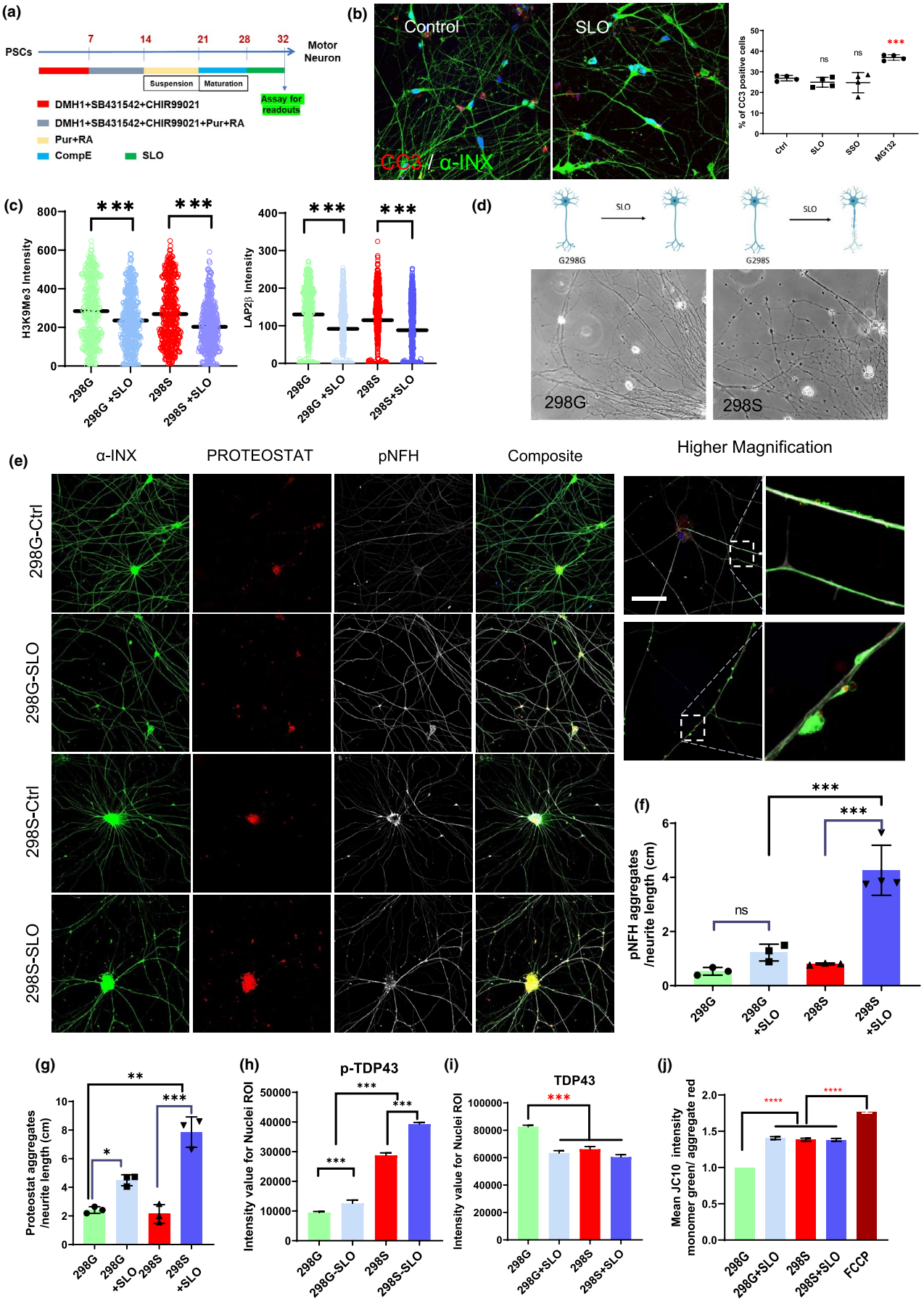
(a)
PSCs
7
14
21
28
32
Motor Neuron
Suspension
Maturation
Assay for readouts
DMH1+SB431542+CHIR99021
DMH1+SB431542+CHIR99021+Pur+RA
Pur+RA
CompE
SLO
(b)
Control
SLO
CC3 / α-INX
% of CC3 positive cells
ns
ns
***
Ctrl
SLO
SSO
MG132
(c)
H3K9Me3 Intensity
LAP2β Intensity
***
298G
298G +SLO
298S
298S +SLO
(d)
SLO
G298G
G298S
298G
298S
(e)
α-INX
PROTEOSTAT
pNFH
Composite
Higher Magnification
298G-Ctrl
298G-SLO
298S-Ctrl
298S-SLO
(f)
pNFH aggregates /neurite length (cm)
ns
***
(g)
Proteostat aggregates /neurite length (cm)
(h)
p-TDP43
Intensity value for Nuclei ROI
(i)
TDP43
Intensity value for Nuclei ROI
(j)
Mean JC10 intensity monomer green/ aggregate red
****
FCCP

FIGURE 6 Phenotype presentation by SLO-treated motor neurons derived from *TARDBP* mutant iPSCs. (a) Differentiation protocol used for generating MNs from TDP-43 298S mutant and 298G isogenic iPSCs. (b) Immunostaining and quantification for cleaved caspase 3 and alpha internexin proteins in cultured MNs treated with SLO, SSO and MG-132, at Day 28. (c) High-content imaging for H3K9M3 and Lap2β in both TDP43 298G isogenic control and 298S mutant following SLO treatment (Mean of SLO treatment compared to the control group with DMSO). (d) Representative phase contrast image of MN cultures from both control and mutant ALS neurons treated with SLO. (e) Immunostaining images for alpha-internexin, Proteostat, phosphorylated neurofilament heavy proteins in control and mutant MNs treated with SLO; right panel shows higher magnification images of control and mutant MNs treated with SLO (Scale bar = 200 μm, for higher magnification images scale bar = 50 μm). (f) Quantification result for phosphorylated neurofilament aggregates and (g) Proteostat-positive protein aggregations. (h) Quantification of phosphorylated TDP43 protein in the nuclei area across all groups and also (i) quantified nuclear TDP43 protein expression for both 298G, S neurons and SLO-treated neurons. (j) Mitochondrial membrane potential (JC10 assay) of ALS-iPSC-derived MNs treated with SLO compared to the healthy isogenic control cells and isogenic cells treated with FCCP. ($n = 3$, ns: not significant, $^{*}p < 0.05$, $^{**}p < 0.01$, $^{***}p < 0.001$ one-way ANOVA with Dunnett's multiple comparison test, for JC10 assay data were collected using 15,000 cells per group from three independent experiments. Statistical analysis was performed using one-way ANOVA, Tukey post hoc test ($^{****}p < 0.001$))

alkylation pathways; all related to cell division and telomere attrition. Surprisingly, none of the sirtuin inhibitors induced senescence in fibroblasts or neurons despite their effects on aging (Bonda et al., 2011; Satoh et al., 2017). This may reflect differences between cell types or insufficient treatment with the inhibitors.

In post-mitotic cells like neurons, protein quality control, including proteasome and autophagy processing, is more important in CS progression (Pan et al., 2008; Scotter et al., 2014; Zhang et al., 2017). This is reflected in our study showing the powerful CS-inducing effect of autophagy inhibitors (SBI-0206965). Faulty autophagosomes could not clear impaired mitochondria and unfolded protein debris, leading to lack of mitochondrial turnover and producing more oxidative stress (He et al., 2013; Wyss-Coray, 2016). Oxidative stress generates ROS and accounts for higher DNA mutations, which is ultimately related to CS (Campos et al., 2014; Lo Sardo et al., 2017). Similarly, we found that inhibition of DNA glycosylase (*OGG1*), important in detecting and removing oxidized nucleotides in genomic DNA, exacerbates CS phenotype in neurons but not in fibroblasts. Two of the three small molecules in SLO, DNA glycosylase inhibitor (O151) and HIV protease inhibitor (Lopinavir), modulate CS phenotypes in neurons, indicating that base excision repair (BER) pathway is critical for neuronal health and is linked to neurodegenerative diseases (Leandro et al., 2015; Maynard et al., 2015). Lopinavir also inhibits ZMPSTE24 (Coffinier et al., 2007; Mehmood et al., 2016), thereby blocking lamin A biogenesis and leading to an accumulation of prelamin A. ZMPSTE24 deficiency in humans causes an accumulation of prelamin A and leads to lipodystrophy and premature aging (Afonso et al., 2016; Spear et al., 2018; Wang et al., 2016), which perhaps causes senescence phenotype in our cultured neurons. We used three different endopeptidase inhibitors Phosphoramidone (a general metalloendopeptidase), Lopinavir (zinc metalloprotease inhibitor), and GGTI-298 (a geranylgeranyltransferase I (GGTase I) inhibitor), and only Lopinavir induced senescence in cortical neurons in all three markers. Interestingly, none of the endopeptidase inhibitors induced senescence phenotype in fibroblasts, indicating that neurons are more sensitive to the activity of endopeptidase, perhaps for the processing of other lamin proteins rather than just for Lamin A (Jung et al., 2012; Yang et al., 2015).

Information on CS derives largely from studies on mitotic cells. The gene expression pattern of our SLO-treated neurons, revealed by transcriptomic analysis, resembles that of iNs and aged brain. In particular, our in-vitro neuronal senescence system, despite the lack of many other cell types that are normally present in the human brain, resembles the aging cortex samples as indicated by the substantial overlap of age-related transcripts between our CIS neurons and aged human brain tissues (Wang et al., 2018). These transcription profiles may be more specific to CS in neurons. For example, transcripts that are involved in neurexin/neuroligin complexes at synaptic membrane assembly and neurotransmitter release from GABA, glutamate, and cholinergic systems are common between aged brains and SLO-induced senescence. Neurexin expression declines with age and causes decrease in synaptic density and cognitive decline (Konar et al., 2016; Kumar & Thakur, 2015). Other transcripts like CREB regulated transcription coactivator 1 (CRTC1) transcription coactivator of CREB1 (Paramanik & Thakur, 2013), which show significant change in our SLO-treated cortical neurons, also contribute to brain aging and neuronal senescence. Some of other molecules such as p62 (SQSTM1) have multiple function and contribute to neurodegeneration by binding to the ubiquitin molecules that are marked for degradation and by binding to autophagy molecule LC3-II (Ma et al., 2019). In addition, our CIS neurons share several histone variants with the progerin effect in the progeria syndrome. Histone variants are one of the most affected transcripts during CIS in the cortical neurons. Histone variant exchange, by regulating expression of age-related genes (Gevry et al., 2007) and/or chromatin organization (Flex et al., 2019), is one of the mechanisms behind CS and aging. Thus, our CIS recapitulates aspects of premature aging effects primarily at the epigenetic level.

A major driving force behind the development of CIS is to enable effective and reliable modeling of age-related diseases using human stem cells. We and others have shown that some aspects of neurodegenerative changes such as ALS may be recapitulated by strictly controlling the neuronal differentiation process, prolonged maturation, and undergoing stress (including culturing under a basal condition without trophic factors and medium changes; Chen et al., 2014; Qian et al., 2017; Sances et al., 2016). Such manipulations over a long term add variables to the system, making stem

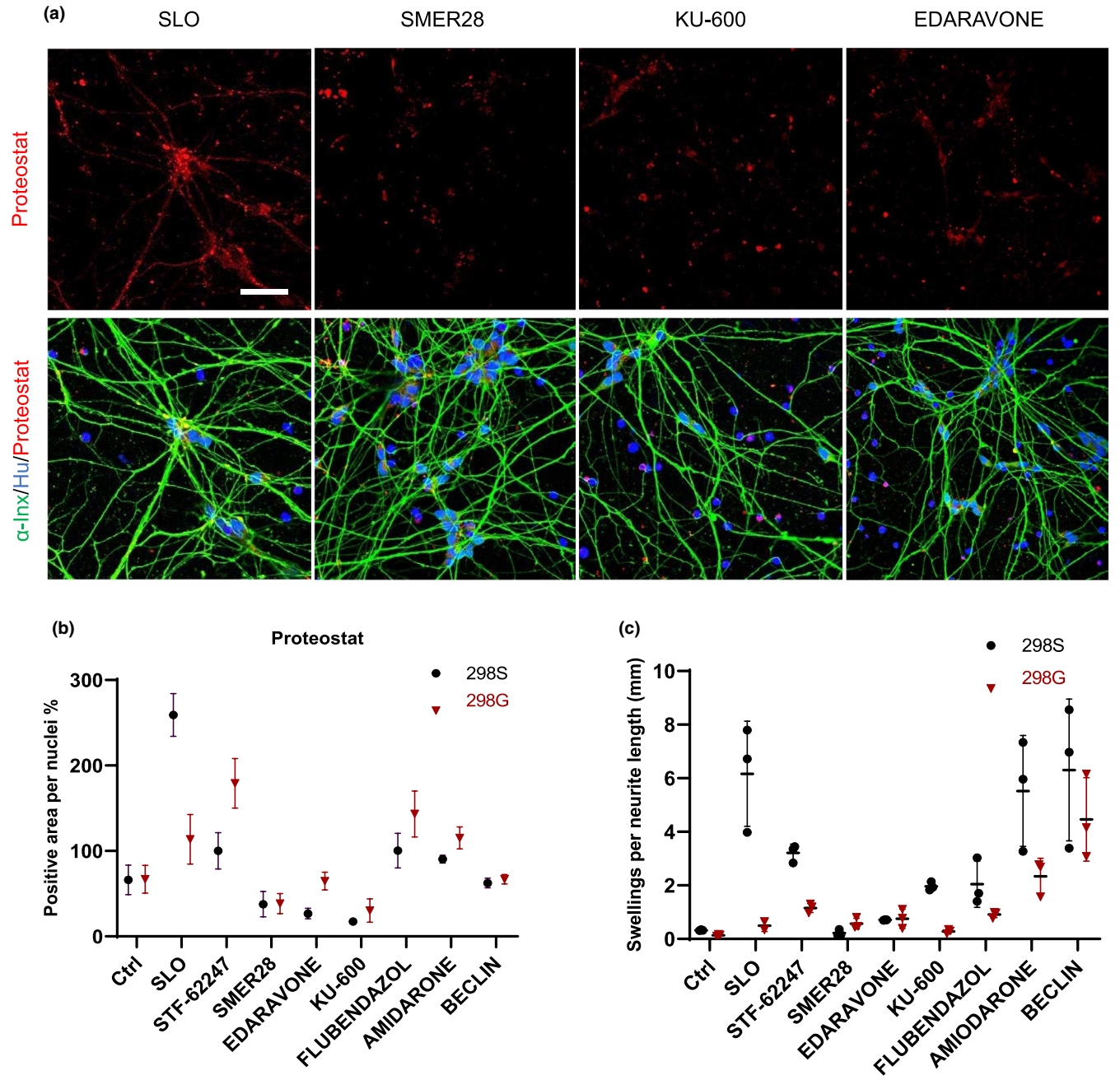

FIGURE 7 Testing molecules that rescue the disease phenotype in ALS MNs. (a) MNs from TDP-43 G298S mutant and G298G isogenic iPSCs treated with SLO to induce CS phenotypes and 24hr later candidate molecules SMER28, EDARAVONE, and KU-60019 were added to the culture and cells stained with Proteostat dye for protein aggregation and alphaInternexin for visualizing neurites. (b) Quantification of immunostaining images positive for Proteostat and (c) neurite swellings. (n = 3, Scale bar=100 μm)

cell-based disease modeling more difficult. MNs from patients with TARDBP mutations have increased levels of soluble and detergent-resistant TDP-43 and show decreased cell survival, suggesting that this model is representative for ALS pathology (Bilican et al., 2012; Fujimori et al., 2018). However, neither increase in insoluble TDP43 nor its mislocalization phenotype is repeated in a recent study (Klim et al., 2019). Similarly, dopamine neurons from PD iPSCs exhibited mitochondrial dysfunction and oxidative stress, changes in neurite growth and morphology, synaptic connectivity, and lysosomal dysfunction (Kouroupi et al., 2017; Monzio Compagnoni et al., 2018; Reinhardt et al., 2013; Sanchez-Danes et al., 2012), but hallmark pathology like protein aggregation and Lewy body formation are rarely observed (Kouroupi et al., 2017; Mishima et al., 2018; Monzio Compagnoni et al., 2018; Reinhardt et al., 2013). These inconsistencies may be due to the different protocols used and the long-term cultures that are necessary to mature the stem cell-derived neurons. The current CIS approach enables an early and consistent presentation of disease-relevant phenotypes, including protein aggregation and axonal degeneration in TDP43 mutant MNs. Since the cocktails induce CS in different neuronal types, it is likely that

the CIS approach may promote phenotypic presentation in other age-related diseases using iPSCs.

Since our CIS method enables faster and consistent presentation of disease phenotypes from iPSC-derived neurons, it is also useful for establishment of drug testing platforms. As a proof of principle test, we found that the current ALS medication Edaravone and one of the many autophagy activators SMER28 but not others mitigate protein aggregation and neurite swelling in ALS iPSC-derived MNs, highlighting the utility of the system.

3.1 | Limitations of the study

Our CIS method induces CS in a short period (after 4 days of treatment) without a need of genetic manipulation. However, it may be desirable to induce senescence more slowly for certain phenotypic presentation, which we have not tested. While the cocktails induce CS in multiple cell types including cortical neurons and MNs, we have not examined other disease models. The cocktails were developed by screening a relatively small pool of molecules, suggesting that other molecules, especially those affecting similar pathways, may also induce CS.

4 | EXPERIMENTAL MODEL AND SUBJECT DETAILS

4.1 | Neuronal differentiation from hPSCs

These studies were approved by the stem cell research oversight committee, University of Wisconsin-Madison. Human embryonic stem cells (H9 or WA09, WiCell), H9-GFP (AAVS1CAG-eGFP) cells, and TARDBP mutant (G298S; Sun et al., 2018) and isogenic (control) induced pluripotent stem cells (iPSCs) were grown on Matrigel with Essential-8 medium (Stemcell Technologies) to 25% confluency. For cortical neuron differentiation, the fifth day cultures of hPSCs were treated with Accutase and the dissociated single cells were cultured in the neural differentiation medium (DMEM/F12:Neurobasal 1:1 + 1× N2 Supplement + 1 mM L-Glutamax) with the SMAD inhibitors SB431542 (Stemgent), DMH-1 (Tocris) (both at 2 μM), and Rho kinase inhibitor (Tocris; overnight) as spheres (embryoid bodies) for 7 days. On Day 8, neural spheres were patterned to dorsal forebrain (cerebral cortical) progenitors with the smoothened antagonist cyclopamine (Stemgent, 2 μM) and FGF2 (R&D, 10 ng/ml) for 7 days. On Day 14, neural progenitors were dissociated with Accutase to single cells and plated on Laminin coated plates in the maturation media (DMEM/F12/Neurobasal 50%/50%, 1× B27 Supplement, 1× non-essential amino acids, 1× Glutamax) supplemented with Compound E (0.1 μM, TOCRIS) for final maturation until assay time. For MN differentiation, we used our previous published protocol with no further modification (Du et al., 2015). For SLO experiments and autophagy activation MNs treated 4 days after maturation (Day 25) with SLO molecules and autophagy activators and other molecules added 24 h later and neurons cultured for another 3 days and analyzed at Day 29.

4.2 | Direct conversion of human fibroblasts into iNs

Primary human dermal fibroblasts (WC-04-05-CO-DG, 72-year-old male, WC-60-07-CO-CMN neonatal male, WC-03-06-CO-DG, 62-year-old female, and WC-59-07-CO-CMN, neonatal female, neonatal fibroblasts from WiCell and aged fibroblasts from David Gamm's lab) were cultured in DMEM containing 15% tetracycline-free fetal bovine serum and 0.1% NEAA (Life Technologies), transduced with lentiviral particles for EtO and XTPNgn2: 2A:Ascl1 (N2A), and expanded in the presence of G418 (200 mg/ml; Life Technologies) and puromycin (1 mg/ml; Sigma-Aldrich). For iN conversion, we followed the previously published protocol (Mertens et al., 2015). We used neuron conversion (NC) medium based on DMEM:F12/Neurobasal (1:1) for 3 weeks. NC contained the following supplements: N2 supplement, B27 supplement (both 1×; GIBCO), doxycycline (2 μg/ml; Sigma-Aldrich), Laminin 1 μg/ml; (Life Technologies), dibutyryl cAMP (400 μg/ml; Sigma-Aldrich), human recombinant Noggin (150 ng/ml; R&D), LDN-193189 (0.5 μM; Cayman Chemicals) and A83-1 (0.5 μM; Stemgent), CHIR99021 (3 μM; LC Laboratories) and SB-431542 (10 μM; Cayman Chemicals). Medium was changed every third day. For further maturation, iNs were cultured in DMEM:F12/Neurobasal-based neural maturation media (NM) containing N2, B27, GDNF, BDNF (both 20 ng/ml; R&D), dibutyryl cAMP (400 μg/ml; Sigma-Aldrich), doxycycline (2 μg/ml; Sigma-Aldrich), and laminin (1 μg/ml; Life Technologies).

Converted neurons in 96-well plates were used for immunostaining without further purification.

4.3 | Immunofluorescent staining and microscopy

Cells were fixed for 20 min with 4% paraformaldehyde in PBS at a room temperature. Samples were blocked with 4% donkey serum and 0.2% Tween20 for 1 h. Primary antibodies were diluted in 4% donkey serum and 0.1% Tween20 and applied to samples overnight at 4°C. Samples were washed with PBS, incubated with fluorescein-conjugated secondary antibodies for 1 h at room temperature, and counterstained with Hoechst for 20 min. Samples were imaged on a Nikon A1s confocal microscope (Nikon). For measuring neurite length and swellings, images were processed with Fiji software (Schindelin et al., 2012). First, a threshold was set for images to select all cell processes; then, neurites were skeletonized. For analyzing the skeletonized neurites prune cycle method were used and parameters set to the shortest branch and end points eliminated to prune ends. Then, total brunch length was calculated for labeled skeletons (total branch length in pixel/10,000 = branch length in cm) and for aggregates per neurites length total number of aggregates were divided by the branch length.

The following primary antibodies were used:

Antibody	Species	Catalog no.	Company	Dilution
TDP43	Rabbit	10782-2-AP	Proteintech Group, Inc.	1000
phospho-TDP43	Rat	MABN14	MilliporeSigma	500
P-SCG10	Rabbit	STJ91270	St. John's Lab	300
H3K9Me3 antibody	Rabbit	ab176916	abcam	5000
CHAT antibody	Goat	AB144P	Chemicon	1000
HB9	Mouse	81.5C10	DSHB	50
TUBB3	Rabbit	PRB-435P	Covance	10,000
MAP2	Mouse	M1406	Sigma	1000
Lamp-2	Mouse	NBP2-22217	Novus Biologicals	250
Lamin B1 antibody	Rabbit	ab16048	Abcam	1000
Lamin B2 antibody	Mouse	ab8983	Abcam	500
HP1γ antibody	Rabbit	2619	Cell Signaling	1000
HP1γ antibody	Mouse	MABE656	Millipore	500
LAP2β	Mouse	611000	BD Biosciences	50
Lamin A + C antibody	Rabbit	ab133256	abcam	500
H2A.X	Mouse	05-636	Upstate (EMD Millipore)	500
Alpha-Internexin	Rabbit	AB40758	abcam	500
Cleaved Caspase-3	Rabbit	9661S	Cell signaling	300
PhosphoDetect™ Anti-Neurofilament H	Mouse	NE1022	Millipore-Sigma	2000
Proteostat	NA	ENZ-51023	Enzo	1000
SOX1	Goat	AF3369	R&D systems	2000
OTX2	Goat	AF1979	R&D systems	2000

4.4 | High-content imaging

For measuring cell population, fluorescence intensity, apoptosis, and intensity of H3K9Me3, Lamin B2, Lap2β, and HP1γ, cells were plated in 96-well imaging plates (18000 cells per well, CELL CARRIER) and treated with different molecules (Table S1). After staining, images were analyzed using the high-content cellular analysis system Operetta (Perkin Elmer). A set of 60 fields was collected from each well (total of three wells per treatment) using the 40× objective, resulting in over 10,000 cells being scored per well. In our analysis workflow, we first identified the nuclei based on default protocol B and calculated the intensity and morphology properties for each nucleus by gating out nuclei with a roundness of below 0.75 and intensities above 1500 for removing extremely bright nuclei (dead cells). We then calculated the signal intensity for each protein in different channels separately. For quantification of H3K9Me3, Lamin B2, and Lap2β intensity in directly reprogrammed neurons, we identified the cytoplasm based on the βIII-tubulin staining surrounding each selected nucleus and quantified the expression of markers in βIII-tubulin-positive population. All raw data were exported and analyzed with GraphPad Prism (GraphPad Software).

4.5 | RNA-seq procedure

Cortical neurons differentiated for 7 days and then treated with SLO for 5 days were collected for RNAseq analysis. All experiments were run three times, and RNA was extracted from all samples (3 biological replicates and 3 technical replicates) using the RNeasy Plus Mini kit (Qiagen) following manufacturer's instructions. RNA quality was assessed using an Agilent RNA PicoChip with all samples passing QC. Sample libraries were prepared using poly-A selection using an Illumina TruSeq RNAv2 kit following manufacturer's instructions. Prepared libraries were sequenced for 101-bp single-read and performed on an Illumina HiSeq to a read depth of >25 million reads per sample by the DNA Sequencing Facility in the University of Wisconsin-Madison Biotechnology Center. FastQC was performed on all samples with every sample passing all quality control measurements.

4.6 | RNA-seq analysis

Differentially expressed genes were identified with a glm function using the edgeR package. A subset of up to 50 of the most differentially expressed genes with a p-value < 0.05 and a log foldchange

greater or less than ±2 were selected according to their FDR rank in the list of DEGs (Du et al., 2015).

Next, both samples and genes were clustered using Euclidean distances. For genes, an additional elbow function was applied to estimate the number of gene clusters present. Calculated relationships are depicted by dendrograms drawn at the top (samples) and to the left (genes) of the heatmap. The gradation of color is determined by a *Z*-score that is computed and scaled across rows of genes normalized by TMM. The *Z*-score of a given expression value is the number of standard-deviations away from the mean of all the expression values for that gene.

The empirical Bayes hierarchical modeling approach EBSeq was used to identify differentially expressed genes across 2 or more conditions. Median normalization technique of DESeq was used to account for differences in sequencing depth. EBSeq calculates the posterior probability (PP) of a gene being in each expression pattern. Genes were declared differentially expressed at a false discovery rate controlled at 100*(1 − α) % if the posterior probability of P1 (EE) is less than 1 − α. Given this list of DE genes, the genes are further classified into each pattern and sorted by PP.

For quantifying the degrees to which genes are associated with aging in the human brain, we performed one-side *t* tests for each gene to determine whether it is significantly positively expressed (i.e., up-regulation) in the aged group (>60 years, $N = 205$) and the young group (<30 years, $N = 128$) of the healthy human brain tissue samples (DLPFC) in the PsychENCODE project (Wang et al., 2018). Then, we used the value of -log10 (*t* test *p*-value) of the gene as "human aging score" to quantify its degree of association with the corresponding group in the human brain. Finally, each gene has two human aging scores to quantify its association with (1) up-regulation in the aged group; (2) up-regulation in the young group.

4.7 | Principal component analysis

For PCA, all the data including cortical neurons RNAseq data, iN data, and PsychENCODE data were first transformed by log10 ($x + 1$). All samples including our SLO and CTRL samples, the aged and young groups in PsychENCODE (as described above), and iNs. combined as a single data matrix (samples by genes) for PCA.

4.8 | Pathway analysis

DEGs from each group were analyzed for differentially regulated pathways using ENRICHR (www.enrichr.org), which utilizes several pathway databases for general pathway analysis. For our analysis, the KEGG and Wikipathway databases were utilized. DEGs were defined as >100 TPM and >twofold change over each of the other groups. Pathways that were statistically significant were highlighted as potential differentially regulated. Only pathways that were found significant in more than one of the three analyses were considered for further evaluation.

4.9 | qRT-PCR

RNA samples were obtained using the RNeasy Plus Mini kit (Qiagen) following manufacturer's instructions. cDNA libraries were constructed using iScript cDNA Synthesis kit (Bio-Rad) using 500 ng of purified RNA from each sample as input following manufacturer's instructions. qRT-PCR was performed on a CFX Connect qPCR machine (Bio-Rad) using iTaq SYBR green supermix (Bio-Rad) and equal amounts of cDNA samples. Results were normalized to GAPDH or 18s rRNA levels using the ΔΔCt method.

4.10 | SA-β galactosidase assay

Fibroblasts were fixed using 1× fixation buffer provided in reagents, and procedure was performed following manufacturer's instructions. Bright-field mages were acquired using a Nikon microscope, and positive cell numbers were calculated using the Fiji software. Positive cells were grouped based on their appearance after β-Gal staining using histogram function (quantity of staining) to the high and moderate.

4.11 | Live and dead cell staining

For the cell toxicity assay, cells were plated in 96-well optical plates at a density of 30,000 cells per well and each three well (experimental replicates) treated with different small molecules for 24 h. Then, cells were washed with PBS and incubated with 1 μM EthD-1 and 1 μM calcein AM for 30 min at RT and imaged using Operetta (Perkin Elmer) and analyzed with Harmony software.

4.12 | Single nucleotide polymorphism (SNP) modification in TARDBP locus

To perform SNP modification, we utilized the single-strand oligonucleotide (ssODN) method. Following sgRNA identification for the site of interest using the crispr.mit.edu design tool, we cloned the sgRNA sequences into the pLentiCRISPR-V1 plasmid from the laboratory of Feng Zhang (not available through Addgene anymore, but V2 version is plasmid #52961) following the protocol provided with the plasmid (Sanjana et al., 2014). Cells were cultured and electroporated as described in Chen et al. (2015). Single hESCs (1×10^7 cells) were electroporated with appropriate combination of plasmids in 500 μl of Electroporation Buffer (KCl 5 mM, $MgCl_2$ 5 mM, HEPES 15 mM, Na_2HPO_4 102.94 mM, NaH_2PO_4 47.06 mM, PH = 7.2) using the Gene Pulser Xcell System (Bio-Rad) at 250 V, 500 μF in a 0.4 cm cuvettes (Phenix Research Products). Cells were electroporated in a cocktail of 15 μg of the pLentiCRISPRV1TDP43 sg14 plasmid and 100 μl of a 10 micromolar ssODN targeting the TDP43 G298S mutant genetic site. This ssODN was non-complementary to the sgRNA sequence and consisted of 141 nucleotides – 70 nucleotides

upstream and 70 nucleotides downstream of the targeted indel generation site (Yang et al., 2013). Following electroporation, cells were plated on MEF feeders in 1.0 μM ROCK inhibitor. At 24- and 72-h post-electroporation, cells were treated with puromycin (0.5 μg/ml, Invitrogen, ant-pr-1) to select for cells containing the pLentiCRISPRV1TDP43 sg14 plasmid. After removal of the puromycin at 96 h, cells were cultured in MEF-conditioned hPSC media until colonies were visible.

For genotyping single-cell generated colonies were manually selected and mechanically disaggregated. Genomic DNA was amplified using Q5 polymerase-based PCR (NEB), and proper clones were determined using sanger sequencing. To identify non-specific genome editing, we analyzed suspected off-target sites for genome modification, using the five highest-likelihood off-target sites predicted by the crispr.mit.edu algorithms.

4.13 | Mitochondrial morphology (Mitotracker) and membrane potential assay (JC-10 assay)

Neuronal progenitors were plated on Cellvis 35 mm glass bottom dishes at 30,000 cells per dish and matured for 7 days. Mitotracker red (M7512, Invitrogen) were added directly to the culture media at final concentrations of 50 nM and incubated for 15 min in the incubator. Cells were then washed three times with phenol-free neurobasal media (pre-warmed to 37°C) and switched to 2 ml of pre-warmed neuronal media. Imaging was performed on a Nikon A1s confocal microscope with live cell chamber incubation. Nikon Elements software were used to acquire images under resonant scanning mode.

Mitochondrial membrane potential assay was performed using JC-10 mitochondrial membrane potential assay kit (ab112134, Abcam). H9-derived Cortical neuron progenitors and 298G and 298S hiPSC-derived MN progenitors were plated at 18000 cells per well in a 96-well imaging plate (Cell carrier). Neurons were treated with SLO (1:1000) at Day 7 for cortical neurons and at Day 4 for MNs. JC-10 assay was performed at Day 11 for cortical neurons and Day 9 for MNs. FCCP (mitochondrial uncoupler) at 2 μm was used as a positive control. Neurons for positive control were treated with FCCP for 30 min at 37°C followed by a wash with the complete neuronal medium. First, JC10 buffer A was added to the neurons and incubated for 30 min at 37°C. Then, both JC10 buffer B and Nucblue live ready reagent (Thermo fisher) were added to the neurons and imaged immediately. Live cell imaging was acquired using high-content microscopy (Operetta- Perkin Elmer). Image analysis was performed using Columbus software. Statistical analysis was made using GraphPad Prism 9.0.

4.14 | MitoSoX staining

Mitosox imaging assay was performed using MitoSOX™ Red Mitochondrial Superoxide Indicator purchased from Thermo Fisher (M36008). MitoSOX red (5 μM) was added to the neurons and incubated for 30 min at 37°C. MitoSOX was removed after 30 min, and Nucblue live ready reagent was added to the neurons and imaged immediately.

4.15 | Immuno blotting

H9-derived cortical neurons were gently scraped off the wells, washed with PBS, and centrifuged at 400 g for 2 mins. Pellets were lysed on ice using RIPA lysis buffer (Cell Signaling) supplemented with Halt Protease and Phosphatase inhibitor cocktail (Thermo Fisher Scientific) and 4-(2-Aminoethyl)benzenesulfonyl fluoride hydrochloride (AEBSF, Sigma). Samples were centrifuged at 22000 g for 20 min at 4°C. Total protein concentrations were measured using Pierce BCA protein assay (Thermo Fisher Scientific). 2× Laemmli sample buffer (Bio-rad) was added to the protein sample and boiled at 95°C for 5 min. Protein samples (10 μg/group) were run on 4%–20% Mini-Protean TGX precast gel (Bio-rad), transferred to polyvinylidene difluoride membranes, blocked with 5% non-fat dry milk, and then incubated with primary antibodies overnight at 4°C. Signals were visualized using horseradish peroxidase-conjugated secondary antibodies and captured with ChemiDoc system. The following primary antibodies were used: LAP2 (1:5000, BD Biosciences), H3K9Me3 (1:5000, Abcam), HP1γ (1:1000, Cell signaling), Lamin B1 (1:5000, Abcam), and P21 (1:1000, Abcam).

4.16 | Statistical analysis

Graphpad (Prism 9) was used for statistical analysis. Unpaired Student's *t* test or one-way ANOVA test with Dunnett's multiple comparison or Tukey's post hoc test was performed.

ACKNOWLEDGEMENTS

We thank D. Moore lab for providing EtO and XTPNgn2: 2A:Ascl1 (N2A) vectors. We are grateful for technical support provided by K.M. Knobel and CMN Core at Waisman center. We would also like to thank R. Bradly, J.R. Jones, Y. Tao, and M. Ayala for their comments and technical support. This study was supported in part by the ALS Association (20-IIP-556), the NIH-NIMH (MH100031), NIH-NINDS (NS086604, NS096282), NIH-NICHD (HD076892), ASAP000301, the Ministry of Education (MOE2018-T2-2-103), and a core grant to the Waisman Center from the NIH-NICHD (U54 HD090256). S--C.Z. acknowledges the Steenbock professorship in Behavioral and Neural Sciences.

CONFLICT OF INTEREST

RNA-seq data have been deposited in the Gene Expression Omnibus (GEO) under accession GSE141028. The authors declare no competing financial interests. Correspondence, and requests for materials should be addressed to S-C.Z. (suchun.zhang@wisc.edu). S-C.Z. is the co-founder of BrainXell, Inc.

AUTHOR CONTRIBUTIONS

A.F. involved in design and conception of the study, writing of manuscript, maintenance, directed differentiation, direct conversion of fibroblasts, establishing of high-content imaging assays, and small molecule screen. S.M. conduct the SLO response in cortical neurons, Western blotting and JC10 MMP assay, wrote the manuscript. L.K contributed to Mitotracker assay and MMP assay. A.J.P. involved in gene targeting of TARDBP in human PS cells and characterization of iPSCs. C.R.K.H. involved in immunostaining, high-content imaging, data interpretation, and editing the manuscript. J.B and J.M.M. involved in RNA sample preparations, immunostaining, and cell toxicity assays. A.B. involved in design and interpretation of small molecule screen and follow-up experiment, writing of manuscript. D.W involved in RNAseq data analysis, comparing RNAseq data to iNs and brain data, and writing of manuscript. SC.Z. involved in design and conception of the study, data interpretation, and writing of manuscript.

DATA AVAILABILITY STATEMENT

The published article includes all datasets generated or analyzed during this study. The datasets supporting this study are available from the lead contact, Dr. Su-Chun Zhang (suchun.zhang@wisc.edu) upon request.

ORCID

Ali Fathi https://orcid.org/0000-0002-1570-8883
Andrew J. Petersen https://orcid.org/0000-0002-3626-816X
Daifeng Wang https://orcid.org/0000-0001-9190-3704

REFERENCES

Afonso, P., Auclair, M., Boccara, F., Vantyghem, M.-C., Katlama, C., Capeau, J., Vigouroux, C., & Caron-Debarle, M. (2016). LMNA mutations resulting in lipodystrophy and HIV protease inhibitors trigger vascular smooth muscle cell senescence and calcification: Role of ZMPSTE24 downregulation. *Atherosclerosis*, *245*, 200–211. https://doi.org/10.1016/j.atherosclerosis.2015.12.012

Baker, D. J., & Petersen, R. C. (2018). Cellular senescence in brain aging and neurodegenerative diseases: Evidence and perspectives. *Journal of Clinical Investigation*, *128*, 1208–1216. https://doi.org/10.1172/JCI95145

Bickford, P. C., Flowers, A., & Grimmig, B. (2017). Aging leads to altered microglial function that reduces brain resiliency increasing vulnerability to neurodegenerative diseases. *Experimental Gerontology*, *94*, 4–8. https://doi.org/10.1016/j.exger.2017.01.027

Bilican, B., Serio, A., Barmada, S. J., Nishimura, A. L., Sullivan, G. J., Carrasco, M., Phatnani, H. P., Puddifoot, C. A., Story, D., Fletcher, J., Park, I. H., Friedman, B. A., Daley, G. Q., Wyllie, D. J., Hardingham, G. E., Wilmut, I., Finkbeiner, S., Maniatis, T., Shaw, C. E., & Chandran, S. (2012). Mutant induced pluripotent stem cell lines recapitulate aspects of TDP-43 proteinopathies and reveal cell-specific vulnerability. *Proceedings of the National Academy of Sciences of the United States of America*, *109*, 58035808. https://doi.org/10.1073/pnas.1202922109

Bonda, D. J., Lee, H., Camins, A., Pallàs, M., Casadesus, G., Smith, M. A., & Zhu, X. (2011). The sirtuin pathway in ageing and Alzheimer disease: Mechanistic and therapeutic considerations. *The Lancet Neurology*, *10*, 275–279. https://doi.org/10.1016/s14744422(11)70013-8

Campos, P. B., Paulsen, B. S., & Rehen, S. K. (2014). Accelerating neuronal aging in in vitro model brain disorders: A focus on reactive oxygen species. *Frontiers in Aging Neuroscience*, *6*, 292. https://doi.org/10.3389/fnagi.2014.00292

Chen, H., Qian, K., Du, Z., Cao, J., Petersen, A., Liu, H., Blackbourn, L. W., Huang, C.- T.-L., Errigo, A., Yin, Y., Lu, J., Ayala, M., & Zhang, S.-C. (2014). Modeling ALS with iPSCs reveals that mutant SOD1 misregulates neurofilament balance in motor neurons. *Cell Stem Cell*, *14*, 796–809. https://doi.org/10.1016/j.stem.2014.02.004

Chen, Y., Cao, J., Xiong, M., Petersen, A. J., Dong, Y., Tao, Y., Huang, C. T., Du, Z., & Zhang, S. C. (2015). Engineering human stem cell lines with inducible gene knockout using CRISPR/Cas9. *Cell Stem Cell*, *17*(2), 233–244. https://doi.org/10.1016/j.stem.2015.06.001

Childs, B. G., Durik, M., Baker, D. J., & van Deursen, J. M. (2015). Cellular senescence in aging and agerelated disease: From mechanisms to therapy. *Nature Medicine*, *21*, 1424–1435. https://doi.org/10.1038/nm.4000

Coffinier, C., Hudon, S., Farber, E., Chang, S., Hrycyna, C., Young, S., & Fong, L. (2007). HIV protease inhibitors block the zinc metalloproteinase ZMPSTE24 and lead to an accumulation of prelamin A in cells. *Proceedings of the National Academy of Sciences USA*, *104*, 13432–13437. https://doi.org/10.1073/pnas.0704212104

Coppe, J. P., Rodier, F., Patil, C. K., Freund, A., Desprez, P. Y., & Campisi, J. (2011). Tumor suppressor and aging biomarker p16(INK4a) induces cellular senescence without the associated inflammatory secretory phenotype. *Journal of Biological Chemistry*, *286*, 36396–36403. https://doi.org/10.1074/jbc.M111.257071

Dreesen, O., & Stewart, C. L. (2011). Accelerated aging syndromes, are they relevant to normal human aging? *Aging*, *3*, 889–895. https://doi.org/10.18632/aging.100383

Du, Z. W., Chen, H., Liu, H., Lu, J., Qian, K., Huang, C. L., Zhong, X., Fan, F., & Zhang, S. C. (2015). Generation and expansion of highly pure motor neuron progenitors from human pluripotent stem cells. *Nature Communications*, *6*, 6626. https://doi.org/10.1038/ncomms7626

Duncan, G. W. (2011). The aging brain and neurodegenerative diseases. *Clinics in Geriatric Medicine*, *27*, 629–644. https://doi.org/10.1016/j.cger.2011.07.008

Flex, E., Flex, E., Martinelli, S., Van Dijck, A., Ciolfi, A., Cecchetti, S., Coluzzi, E., Pannone, L., Andreoli, C., Radio, F. C., Pizzi, S., Carpentieri, G., Bruselles, A., Catanzaro, G., Pedace, L., Miele, E., Carcarino, E., Ge, X., Chijiwa, C., … Carcar, E. (2019). Aberrant function of the C-terminal tail of HIST1H1E accelerates cellular senescence and causes premature aging. *American Journal of Human Genetics*, *105*, 493–508. https://doi.org/10.1016/j.ajhg.2019.07.007

Fujimori, K., Ishikawa, M., Otomo, A., Atsuta, N., Nakamura, R., Akiyama, T., Hadano, S., Aoki, M., Saya, H., Sobue, G., & Okano, H. (2018). Modeling sporadic ALS in iPSC-derived motor neurons identifies a potential therapeutic agent. *Nature Medicine*, *24*, 1579–1589. https://doi.org/10.1038/s41591-0180140-5

Gevry, N., Chan, H. M., Laflamme, L., Livingston, D. M., & Gaudreau, L. (2007). p21 transcription is regulated by differential localization of histone H2A.Z. *Genes & Development*, *21*, 1869–1881. https://doi.org/10.1101/gad.1545707

He, L. Q., Lu, J. H., & Yue, Z. Y. (2013). Autophagy in ageing and ageing-associated diseases. *Acta Pharmacologica Sinica*, *34*, 605–611. https://doi.org/10.1038/aps.2012.188

Hernandez-Segura, A., Nehme, J., & Demaria, M. (2018). Hallmarks of cellular senescence. *Trends in Cell Biology*, *28*, 436–453. https://doi.org/10.1016/j.tcb.2018.02.001

Jung, H. J., Coffinier, C., Choe, Y., Beigneux, A., Davies, B., Yang, S., Barnes, R. H., Hong, J., Sun, T., Pleasure, S., Young, S., & Fong, L. (2012). Regulation of prelamin A but not lamin C by miR-9, a brain-specific microRNA. *Proceedings of the National Academy of Sciences*, *109*, E423–E431. https://doi.org/10.1073/pnas.1111780109

Kim, Y., Zheng, X., Ansari, Z., Bunnell, M. C., Herdy, J. R., Traxler, L., Lee, H., Paquola, A. C. M., Blithikioti, C., Ku, M., Schlachetzki, J. C. M., Winkler, J., Edenhofer, F., Glass, C. K., Paucar, A. A., Jaeger, B. N., Pham, S., Boyer, L., Campbell, B. C., … Gage, F. H. (2018). Mitochondrial aging defects emerge in directly reprogrammed human neurons due to their metabolic profile. *Cell Reports*, *23*, 2550–2558. https://doi.org/10.1016/j.celrep.2018.04.105

Klim, J. R., Williams, L. A., Limone, F., Guerra San Juan, I., Davis-Dusenbery, B. N., Mordes, D. A., Burberry, A., Steinbaugh, M. J., Gamage, K. K., Kirchner, R., Moccia, R., Cassel, S. H., Chen, K., Wainger, B. J., Woolf, C. J., & Eggan, K. (2019). ALS-implicated protein TDP-43 sustains levels of STMN2, a mediator of motor neuron growth and repair. *Nature Neuroscience*, *22*, 167–179. https://doi.org/10.1038/s41593-018-0300-4

Konar, A., Singh, P., & Thakur, M. K. (2016). Age-associated cognitive decline: Insights into molecular switches and recovery avenues. *Aging and Disease*, *7*, 121–129. https://doi.org/10.14336/AD.2015.1004

Kouroupi, G., Taoufik, E., Vlachos, I. S., Tsioras, K., Antoniou, N., Papastefanaki, F., Chroni-Tzartou, D., Wrasidlo, W., Bohl, D., Stellas, D., Politis, P. K., Vekrellis, K., Papadimitriou, D., Stefanis, L., Bregestovski, P., Hatzigeorgiou, A. G., Masliah, E., & Matsas, R. (2017). Defective synaptic connectivity and axonal neuropathology in a human iPSC-based model of familial Parkinson's disease. *Proceedings of the National Academy of Sciences of the United States of America*, *114*, E3679E3688. https://doi.org/10.1073/pnas.1617259114

Kumar, D., & Thakur, M. K. (2015). Age-related expression of Neurexin1 and Neuroligin3 is correlated with presynaptic density in the cerebral cortex and hippocampus of male mice. *Age*, *37*, 17. https://doi.org/10.1007/s11357-015-9752-6

Kyng, K. J., May, A., Kolvraa, S., & Bohr, V. A. (2003). Gene expression profiling in Werner syndrome closely resembles that of normal aging. *Proceedings of the National Academy of Sciences USA*, *100*, 12259–12264. https://doi.org/10.1073/pnas.2130723100

Lapasset, L., Milhavet, O., Prieur, A., Besnard, E., Babled, A., Aït-Hamou, N., Leschik, J., Pellestor, F., Ramirez, J.-M., De Vos, J., Lehmann, S., & Lemaitre, J.-M. (2011). Rejuvenating senescent and centenarian human cells by reprogramming through the pluripotent state. *Genes & Development*, *25*, 2248–2253. https://doi.org/10.1101/gad.173922.111

Leandro, G. S., Sykora, P., & Bohr, V. A. (2015). The impact of base excision DNA repair in age-related neurodegenerative diseases. *Mutation Research*, *776*, 31–39. https://doi.org/10.1016/j.mrfmmm.2014.12.011

Lo Sardo, V., Ferguson, W., Erikson, G. A., Topol, E. J., Baldwin, K. K., & Torkamani, A. (2017). Influence of donor age on induced pluripotent stem cells. *Nature Biotechnology*, *35*, 69–74. https://doi.org/10.1038/nbt.3749

Lopez-Otin, C., Blasco, M. A., Partridge, L., Serrano, M., & Kroemer, G. (2013). The hallmarks of aging. *Cell*, *153*, 1194–1217. https://doi.org/10.1016/j.cell.2013.05.039

Ma, S., Attarwala, I. Y., & Xie, X. Q. (2019). SQSTM1/p62: A potential target for neurodegenerative disease. *ACS Chemical Neuroscience*, *10*, 2094–2114. https://doi.org/10.1021/acschemneuro.8b00516

Madabhushi, R., Pan, L., & Tsai, L. H. (2014). DNA damage and its links to neurodegeneration. *Neuron*, *83*, 266–282. https://doi.org/10.1016/j.neuron.2014.06.034

Maynard, S., Fang, E. F., Scheibye-Knudsen, M., Croteau, D. L., & Bohr, V. A. (2015). DNA damage, DNA repair, aging, and neurodegeneration. *Cold Spring Harbor Perspectives in Medicine*, *5*, 1–18. https://doi.org/10.1101/cshperspect.a025130

Mehmood, S., Marcoux, J., Gault, J., Quigley, A., Michaelis, S., Young, S. G., Carpenter, E. P., & Robinson, C. V. (2016). Mass spectrometry captures off-target drug binding and provides mechanistic insights into the human metalloprotease ZMPSTE24. *Nature Chemistry*, *8*, 1152–1158. https://doi.org/10.1038/nchem.2591

Menendez, J. A., Vellon, L., Oliveras-Ferraros, C., Cufi, S., & Vazquez-Martin, A. (2011). mTOR-regulated senescence and autophagy during reprogramming of somatic cells to pluripotency: A roadmap from energy metabolism to stem cell renewal and aging. *Cell Cycle*, *10*, 36583677. https://doi.org/10.4161/cc.10.21.18128

Mertens, J., Paquola, A. C. M., Ku, M., Hatch, E., Böhnke, L., Ladjevardi, S., McGrath, S., Campbell, B., Lee, H., Herdy, J. R., Gonçalves, J. T., Toda, T., Kim, Y., Winkler, J., Yao, J., Hetzer, M. W., & Gage, F. H. (2015). Directly reprogrammed human neurons retain aging-associated transcriptomic signatures and reveal age-related nucleocytoplasmic defects. *Cell Stem Cell*, *17*, 705–718. https://doi.org/10.1016/j.stem.2015.09.001

Mertens, J., Reid, D., Lau, S., Kim, Y., & Gage, F. H. (2018). Aging in a dish: iPSC-derived and directly induced neurons for studying brain aging and age-related neurodegenerative diseases. *Annual Review of Genetics*, *52*, 271–293. https://doi.org/10.1146/annurev-genet120417-031534

Miller, J. D., Ganat, Y. M., Kishinevsky, S., Bowman, R. L., Liu, B., Tu, E. Y., Mandal, P. K., Vera, E., Shim, J., Kriks, S., Taldone, T., Fusaki, N., Tomishima, M. J., Krainc, D., Milner, T. A., Rossi, D. J., & Studer, L. (2013). Human iPSC-based modeling of late-onset disease via progerin-induced aging. *Cell Stem Cell*, *13*, 691–705. https://doi.org/10.1016/j.stem.2013.11.006

Mishima, T., Fujioka, S., Fukae, J., Yuasa-Kawada, J., & Tsuboi, Y. (2018). Modeling Parkinson's disease and atypical parkinsonian syndromes using induced pluripotent stem cells. *International Journal of Molecular Sciences*, *19*, 1–18. https://doi.org/10.3390/ijms19123870

Mitsumoto, H., Brooks, B. R., & Silani, V. (2014). Clinical trials in amyotrophic lateral sclerosis: Why so many negative trials and how can trials be improved? *The Lancet Neurology*, *13*, 1127–1138. https://doi.org/10.1016/S1474-4422(14)70129-2

Monzio Compagnoni, G., Kleiner, G., Samarani, M., Aureli, M., Faustini, G., Bellucci, A., Ronchi, D., Bordoni, A., Garbellini, M., Salani, S., Fortunato, F., Frattini, E., Abati, E., Bergamini, C., Fato, R., Tabano, S., Miozzo, M., Serratto, G., Passafaro, M., …, Di Fonzo, A. (2018). Mitochondrial dysregulation and impaired autophagy in iPSC-derived dopaminergic neurons of multiple system atrophy. *Stem Cell Reports*, *11*, 1185–1198. https://doi.org/10.1016/j.stemcr.2018.09.007

Nicholas, C. R., Chen, J., Tang, Y., Southwell, D. G., Chalmers, N., Vogt, D., Arnold, C. M., Chen, Y.-J.- J., Stanley, E. G., Elefanty, A. G., Sasai, Y., Alvarez-Buylla, A., Rubenstein, J. L. R., & Kriegstein, A. R. (2013). Functional maturation of hPSC-derived forebrain interneurons requires an extended timeline and mimics human neural development. *Cell Stem Cell*, *12*, 573–586. https://doi.org/10.1016/j.stem.2013.04.005

Paganoni, S., Cudkowicz, M., & Berry, J. D. (2014). Outcome measures in amyotrophic lateral sclerosis clinical trials. *Clinical Investigation*, *4*, 605–618. https://doi.org/10.4155/cli.14.52

Pan, T., Kondo, S., Le, W., & Jankovic, J. (2008). The role of autophagy-lysosome pathway in neurodegeneration associated with Parkinson's disease. *Brain*, *131*, 1969–1978. https://doi.org/10.1093/brain/awm318

Paramanik, V., & Thakur, M. K. (2013). Role of CREB signaling in aging brain. *Archives Italiennes De Biologie*, *151*, 3342. https://doi.org/10.4449/aib.v151i1.1461

Patterson, M., Chan, D. N., Ha, I., Case, D., Cui, Y., Handel, B. V., Mikkola, H. K. A., & Lowry, W. E. (2012). Defining the nature of human pluripotent stem cell progeny. *Cell Research*, *22*, 178–193. https://doi.org/10.1038/cr.2011.133

Petrova, N. V., Velichko, A. K., Razin, S. V., & Kantidze, O. L. (2016). Small molecule compounds that induce cellular senescence. *Aging Cell*, *15*, 999–1017. https://doi.org/10.1111/acel.12518

Qi, Y., Zhang, X.-J., Renier, N., Wu, Z., Atkin, T., Sun, Z., Ozair, M. Z., Tchieu, J., Zimmer, B., Fattahi, F., Ganat, Y., Azevedo, R., Zeltner, N., Brivanlou, A. H., Karayiorgou, M., Gogos, J., Tomishima, M.,

Tessier-Lavigne, M., Shi, S.-H., & Studer, L. (2017). Combined small-molecule inhibition accelerates the derivation of functional cortical neurons from human pluripotent stem cells. *Nature Biotechnology*, *35*, 154–163. https://doi.org/10.1038/nbt.3777

Qian, K., Huang, H., Peterson, A., Hu, B., Maragakis, N. J., Ming, G. L., Chen, H., & Zhang, S. C. (2017). Sporadic ALS astrocytes induce neuronal degeneration in vivo. *Stem Cell Reports*, *8*, 843–855. https://doi.org/10.1016/j.stemcr.2017.03.003

Rando, T. A., & Chang, H. Y. (2012). Aging, rejuvenation, and epigenetic reprogramming: Resetting the aging clock. *Cell*, *148*, 46–57. https://doi.org/10.1016/j.cell.2012.01.003

Rayess, H., Wang, M. B., & Srivatsan, E. S. (2012). Cellular senescence and tumor suppressor gene p16. *International Journal of Cancer*, *130*, 1715–1725. https://doi.org/10.1002/ijc.27316

Reinhardt, P., Schmid, B., Burbulla, L. F., Schöndorf, D. C., Wagner, L., Glatza, M., Höing, S., Hargus, G., Heck, S. A., Dhingra, A., Wu, G., Müller, S., Brockmann, K., Kluba, T., Maisel, M., Krüger, R., Berg, D., Tsytsyura, Y., Thiel, C. S., …, Sterneckert, J. (2013). Genetic correction of a LRRK2 mutation in human iPSCs links parkinsonian neurodegeneration to ERK-dependent changes in gene expression. *Cell Stem Cell*, *12*, 354–367. https://doi.org/10.1016/j.stem.203.01.008

Rubinsztein, D. C., Marino, G., & Kroemer, G. (2011). Autophagy and aging. *Cell*, *146*, 682–695. https://doi.org/10.1016/j.cell.2011.07.030

Sances, S., Bruijn, L. I., Chandran, S., Eggan, K., Ho, R., Klim, J. R., Livesey, M. R., Lowry, E., Macklis, J. D., Rushton, D., Sadegh, C., Sareen, D., Wichterle, H., Zhang, S.-C., & Svendsen, C. N. (2016). Modeling ALS with motor neurons derived from human induced pluripotent stem cells. *Nature Neuroscience*, *19*, 542–553. https://doi.org/10.1038/nn.4273

Sanchez-Danes, A., Richaud-Patin, Y., Carballo-Carbajal, I., Jiménez-Delgado, S., Caig, C., Mora, S., Di Guglielmo, C., Ezquerra, M., Patel, B., Giralt, A., Canals, J. M., Memo, M., Alberch, J., López-Barneo, J., Vila, M., Cuervo, A. M., Tolosa, E., Consiglio, A., & Raya, A. (2012). Disease-specific phenotypes in dopamine neurons from human iPS-based models of genetic and sporadic Parkinson's disease. *EMBO Molecular Medicine*, *4*, 380395. https://doi.org/10.1002/emmm.201200215

Sanjana, N. E., Shalem, O., & Zhang, F. (2014). Improved vectors and genome-wide libraries for CRISPR screening. *Nature Methods*, *11*(8), 783–784. https://doi.org/10.1038/nmeth.3047

Satoh, A., Imai, S. I., & Guarente, L. (2017). The brain, sirtuins, and ageing. *Nature Reviews Neuroscience*, *18*, 362374. https://doi.org/10.1038/nrn.2017.42

Sawada, M., Sawada, H., & Nagatsu, T. (2008). Effects of aging on neuroprotective and neurotoxic properties of microglia in neurodegenerative diseases. *Neuro-Degenerative Diseases*, *5*, 254–256. https://doi.org/10.1159/000113717

Schindelin, J., Arganda-Carreras, I., Frise, E., Kaynig, V., Longair, M., Pietzsch, T., Preibisch, S., Rueden, C., Saalfeld, S., Schmid, B., Tinevez, J.-Y., White, D. J., Hartenstein, V., Eliceiri, K., Tomancak, P., & Cardona, A. (2012). Fiji: An open-source platform for biological- image analysis. *Nature Methods*, *9*(7), 676–682. https://doi.org/10.1038/nmeth.2019

Scotter, E. L., Vance, C., Nishimura, A. L., Lee, Y. B., Chen, H. J., Urwin, H., Sardone, V., Mitchell, J. C., Rogelj, B., Rubinsztein, D. C., & Shaw, C. E. (2014). Differential roles of the ubiquitin proteasome system and autophagy in the clearance of soluble and aggregated TDP-43 species. *Journal of Cell Science*, *127*, 1263–1278. https://doi.org/10.1242/jcs.140087

Spear, E. D., Hsu, E. T., Nie, L., Carpenter, E. P., Hrycyna, C. A., & Michaelis, S. (2018). ZMPSTE24 missense mutations that cause progeroid diseases decrease prelamin A cleavage activity and/or protein stability. *Disease Models & Mechanisms*, *11*, 1–12. https://doi.org/10.1242/dmm.033670

Sun, X., Song, J., Huang, H., Chen, H., & Qian, K. (2018). Modelling hallmark pathology using motor neurons derived from the family and sporadic amyotropic lateral sclerosis patient-specific iPS cells. *Stem Cell Research & Therapy*, *9*(315), 1–14. https://doi.org/10.1186/s13287-018-1048-1

Vera, E., & Studer, L. (2015). When rejuvenation is a problem: Challenges of modeling late-onset neurodegenerative disease. *Development*, *142*, 3085–3089. https://doi.org/10.1242/dev.120667

Vernadakis, A., & Fleischer-Lambropoulos, H. (2000). Cell culture as a model to study cell-cell interactions during development aging and neurodegenerative diseases. *International Journal of Developmental Neuroscience*, *18*, 139–143. https://doi.org/10.1016/S0736-5748(99)00081-7

Vierbuchen, T., Ostermeier, A., Pang, Z. P., Kokubu, Y., Sudhof, T. C., & Wernig, M. (2010). Direct conversion of fibroblasts to functional neurons by defined factors. *Nature*, *463*, 1035–1041. https://doi.org/10.1038/nature08797

Wang, D., Liu, S., Warrell, J., Won, H., Shi, X., Navarro, F. C. P., Clarke, D., Gu, M., Emani, P., Yang, Y. T., Xu, M., Gandal, M. J., Lou, S., Zhang, J., Park, J. J., Yan, C., Rhie, S. K., Manakongtreecheep, K., Zhou, H., … Gerstein, M. B. (2018). Comprehensive functional genomic resource and integrative model for the human brain. *Science*, *362*, eaat8464. https://doi.org/10.1126/science.aat8464

Wang, Y., Lichter-Konecki, U., Anyane-Yeboa, K., Shaw, J. E., Lu, J. T., Östlund, C., Shin, J. Y., Clark, L. N., Gundersen, G. G., Nagy, P. L., & Worman, H. J. (2016). A mutation abolishing the ZMPSTE24 cleavage site in prelamin A causes a progeroid disorder. *Journal of Cell Science*, *129*, 1975–1980. https://doi.org/10.1242/jcs.187302

Wyss-Coray, T. (2016). Ageing, neurodegeneration and brain rejuvenation. *Nature*, *539*, 180–186. https://doi.org/10.1038/nature20411

Yang, L., Guell, M., Byrne, S., Yang, J. L., De Los Angeles, A., Mali, P., Aach, J., Kim-Kiselak, C., Briggs, A. W., Rios, X., Huang, P.-Y., Daley, G., & Church, G. (2013). Optimization of scarless human stem cell genome editing. *Nucleic Acids Research*, *41*(19), 9049–9061. http://dx.doi.org/10.1093/nar/gkt555

Yang, S. H., Procaccia, S., Jung, H.-J., Nobumori, C., Tatar, A., Tu, Y., Bayguinov, Y. R., Hwang, S. J., Tran, D., Ward, S. M., Fong, L. G., & Young, S. G. (2015). Mice that express farnesylated versions of prelamin A in neurons develop achalasia. *Human Molecular Genetics*, *24*, 2826–2840. https://doi.org/10.1093/hmg/ddv043

Zhang, Y., Chen, X., Zhao, Y., Ponnusamy, M., & Liu, Y. (2017). The role of ubiquitin proteasomal system and autophagy-lysosome pathway in Alzheimer's disease. *Reviews in the Neurosciences*, *28*, 861–868. https://doi.org/10.1515/revneuro-2017-0013

Zhao, H., & Darzynkiewicz, Z. (2013). Biomarkers of cell senescence assessed by imaging cytometry. *Methods in Molecular Biology*, *965*, 83–92. https://doi.org/10.1007/978-1-62703-239-1_5

SUPPORTING INFORMATION

Additional supporting information may be found in the online version of the article at the publisher's website.

How to cite this article: Fathi, A., Mathivanan, S., Kong, L., Petersen, A. J., Harder, C. R. K., Block, J., Miller, J. M., Bhattacharyya, A., Wang, D., & Zhang, S.-C. (2022). Chemically induced senescence in human stem cell-derived neurons promotes phenotypic presentation of neurodegeneration. *Aging Cell*, 21, e13541. https://doi.org/10.1111/acel.13541